Experimental Measurements and Kinetic Modeling of CO/H$_2$/O$_2$/NO$_x$ Conversion at High Pressure

CHRISTIAN LUND RASMUSSEN,[1] JØRN HANSEN,[1] PAUL MARSHALL,[1,2] PETER GLARBORG[1]

[1]Department of Chemical Engineering, Technical University of Denmark, DK-2800 Kgs. Lyngby, Denmark
[2]Department of Chemistry, University of North Texas, Denton, TX 76203–5070

ABSTRACT: This paper presents results from lean CO/H$_2$/O$_2$/NO$_x$ oxidation experiments conducted at 20–100 bar and 600–900 K. The experiments were carried out in a new high-pressure laminar flow reactor designed to conduct well-defined experimental investigations of homogeneous gas phase chemistry at pressures and temperatures up to 100 bar and 925 K. The results have been interpreted in terms of an updated detailed chemical kinetic model, designed to operate also at high pressures. The model, describing H$_2$/O$_2$, CO/CO$_2$, and NO$_x$ chemistry, is developed from a critical review of data for individual elementary reactions, with supplementary rate constants determined from ab initio CBS-QB3 calculations. New or updated rate constants are proposed for important reactions, including OH + HO$_2$ ⇌ H$_2$O + O$_2$, CO + OH ⇌ [HOCO] ⇌ CO$_2$ + H, HOCO + OH ⇌ CO + H$_2$O$_2$, NO$_2$ + H$_2$ ⇌ HNO$_2$ + H, NO$_2$ + HO$_2$ ⇌ HONO/HNO$_2$ + O$_2$, and HNO$_2$(+M) ⇌ HONO(+M). Further validation of the model performance is obtained through comparisons with flow reactor experiments from the literature on the chemical systems H$_2$/O$_2$, H$_2$/O$_2$/NO$_2$, and CO/H$_2$O/O$_2$ at 780–1100 K and 1–10 bar. Moreover, introduction of the reaction CO + H$_2$O$_2$ → HOCO + OH into the model yields an improved prediction, but no final resolution, to the recently debated syngas ignition delay problem compared to previous kinetic models. © 2008 Wiley Periodicals, Inc. Int J Chem Kinet 40: 454–480, 2008

INTRODUCTION

In contrast to empirical models, detailed chemical kinetic models are complex mechanistic models developed from an understanding of the conversion of reactants and formation of products as they actually take place through a chain of elementary reaction steps. Ideally, the nature of a detailed kinetic model may allow extrapolation to reaction conditions outside the range of experimental verification, with an expected accurate response. Throughout decades, this has encouraged a continuous development and refinement of

detailed kinetic models to unravel the complexities of chemical reactions across a wide range of conditions and ultimately to close in on the final solution. The task relies on the availability of well-defined experimental data. Data that fall in the outskirts of previously reported results and, hence, extend the boundaries of model development and verification are of particularly high value.

Well-defined experimental results obtained at high pressure fall into this category. Within recent years, some of the most significant contributions have emerged from flow reactor experiments by Dryer and coworkers, e.g. [1–5], and Dagaut and coworkers, who use a jet-stirred reactor, e.g. [6–8]. These systems are, however, limited to operations within the range of moderately high pressures, up to 20 and 10 bar, respectively. The use of rapid compression machines [9–14] and shock tubes [15–21] has extended this pressure range considerably. However, flow reactor results at very high pressures are still missing despite the relevance to a number of important applications including engines and gas turbines. High pressure is also a driving force in the partial oxidation of natural gas to oxygenated hydrocarbons that play an important role as fuels as well as feedstock in a range of industrial processes.

Because they exhibit relatively high surface to volume ratios, laboratory-scale reactors designed to investigate homogeneous gas phase chemistry typically face the challenge of avoiding heterogeneous interference from the surface material. As a consequence, reactor materials with minimal surface activity are required. Quartz or Pyrex glass are typically preferred even though experiments [22,23] indicate that these are not zero surface activity materials. The brittle nature of these materials, however, imposes a problem when they are subjected to large pressure gradients.

As part of this work, a new high-pressure laminar flow reactor setup was established to conduct well-defined experimental investigations of homogeneous gas phase chemistry at high pressures from 10 to 100 bar. The reaction takes place in a simple tubular quartz reactor with a constant reactor temperature up to 925 K. Experimental results from the conversion of CO/H$_2$/O$_2$/NO$_x$ mixtures are presented. Based on a thorough review, a detailed chemical kinetic model of the CO/H$_2$/O$_2$/NO$_x$ system is presented. It includes improved estimates of selected rate constants from ab initio CBS-QB3 calculations. The CBS-QB3 methodology [24] employs geometries and frequencies computed with density functional theory, at the B3LYP/6-311G(d,p) level of theory for the species considered here. The energy is then obtained by extrapolation of coupled-cluster results to the complete basis set limit. Where the ground electronic state is split by spin–orbit coupling, such as in OH and NO, an empirical energy correction was included. These data are employed in transition state theory to derive rate constants, which in the case of hydrogen transfer reactions include an Eckart tunneling correction. The kinetic model is validated across a pressure range of 1–100 bar using data obtained from the new high-pressure flow reactor as well as previous results from the literature, and the most important reaction pathways are discussed based on the modeling predictions. Finally, the paper discusses the model application to predictions of synthesis gas (CO/H$_2$) ignition times at low temperatures and elevated pressure.

HIGH-PRESSURE FLOW REACTOR

The experimental setup is a new laboratory-scale high-pressure laminar flow reactor designed to approximate plug flow. The system enables well-defined investigations of homogeneous gas phase chemistry at pressures from 10 to 100 bar at temperatures up to 925 K and flow rates of 1–5 NL/min ("N" refers to "normal" conditions at 273.15 K and 1 bar). The reactions take place in a tubular reactor made of quartz (i.d. 8 mm, o.d. 10 mm, lg. 1545 mm). The reactor is enclosed in a TP347 stainless steel tube (i.d. 22 mm, o.d. 38 mm) that acts as a pressure shell. A pressure control system consisting of two thermal mass flow pressure controllers (model 5866 from Brooks Instruments) automatically delivers N$_2$ to the shell-side of the reactor to obtain a pressure similar to that inside the reactor, thus avoiding devastating pressure gradients across the fragile quartz glass. The steel tube is placed horizontally in an Entech tube oven with three individually controlled electrical heating elements that produce an isothermal reaction zone (±5 K) of approximately. 50 cm with steep temperature gradients toward both the inlet and outlet of the reactor tube. This is verified by the measured temperature profiles shown in Fig. 1. The reactor temperature is monitored by type K thermocouples (±2.2 K or 0.75%) positioned inside two steel thermo-pockets placed in the void between the quartz reactor and the steel shell.

A maximum of four different reactant gases are premixed before entering the reactor. The flow rates are regulated by high-pressure digital mass flow controllers (model 5850S from Brooks Instruments). All gases used in the experiments are high purity gases or mixtures with certificated concentrations ($\pm2\%$ uncertainty supplied by Linde Gas AGA). The system is pressurized from the feed gas cylinders. The reactor pressure is monitored before the reactor by a
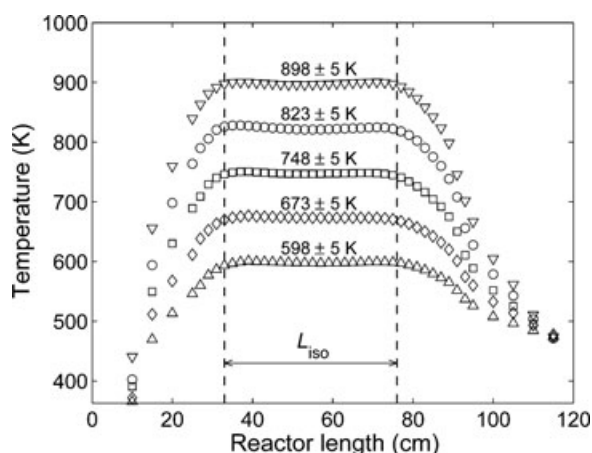
Figure 1   Measured temperature profiles across the reaction zone. The vertical dashed lines delimit the isothermal section of the reactor: $L_{iso} = 43$ cm.

differential pressure transducer (DPharp EJX from Yokogawa) and controlled by a pneumatic pressure valve (Flowserve Kämmer) positioned after the reactor. The system employs two pressure valves designed for steady operation above and below 60 bars, respectively. They are installed in parallel and can be manually selected through a three-way valve. A schematic overview of the system is provided in Fig. 2.

The pressure valves reduce the system pressure to atmospheric level prior to product analysis, which is conducted by an online 6890N Agilent gas chromatograph (GC-TCD/FID from Agilent Technologies) and a NO_x chemiluminescence gas analyzer (CLD 700 EL model from Eco Physics).

All tubing is 1/8 in. stainless steel with Swagelok fittings. The entire downstream section is gently heated

to avoid condensation of potential condensible components before product analysis. This is obtained by covering all tubings and exposed reactor parts with heating cables. The GC has three operational columns (DB1, Porapak N, and Molesieve 13×). Using helium as carrier gas, the GC is used for detection of O_2, CO, and CO_2, while the current configuration does not allow a sufficiently accurate determination of H_2. The overall relative uncertainty of the GC measurements is typically in the range ±5% depending on the applied calibration gases. A similar accuracy is obtained for measurements of NO and NO_2 using the NO_x chemiluminescence gas analyzer.

A unique feature of the system design is the mounting of the quartz reactor inside the steel shell, which prevents the reactant gases from having any contact with surfaces other than the quartz wall during the entire heating, isothermal, and cooling section of the reactor. This is facilitated by two AISI 316 stainless steel flanges positioned at each end of the stainless steel tube. The design is shown in Fig. 3. The reactor enters the flanges through holes that are slightly larger than the quartz tube to make space for the thermal expansion of the steel during heating. The holes turn into small compartments that enclose both ends of the reactor before the 1/4 in. Swagelok connectors that define the reactor inlet and outlet. Inside each compartment, two small AISI 316 steel plates are mounted around the end of the reactor and tightly bolted to the flanges. These plates carry two Viton O-rings that press against the quartz tube and the steel surface of the flanges, respectively, thereby sealing the reactor interior from the pressure shell compartment without damaging the glass during the thermal expansion of the metal. The N_2 inlet to the pressure shell compartment is
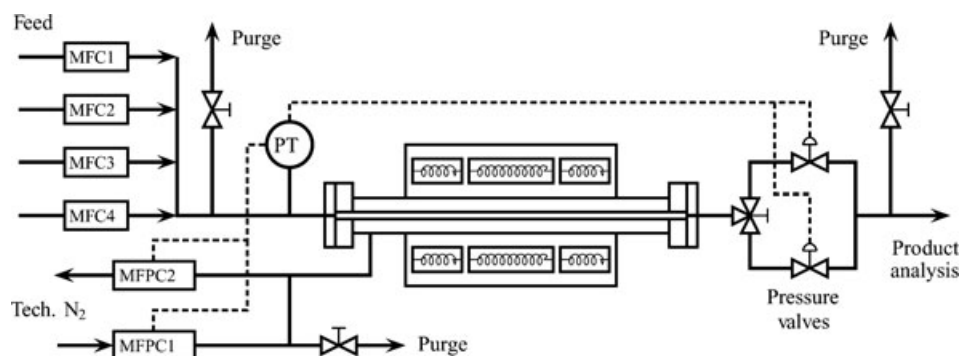
Figure 2   Schematic overview of the system. Reactant gases are premixed from up to four different digital mass flow controllers (MFC) before the reactor inlet. N_2 is supplied to the pressure shell through two thermal mass flow pressure controllers (MFPC). The steel shell with the tubular quartz reactor inside is positioned in an electrically heated oven with three heating elements. Reduction of the pressure to atmospheric level is obtained in the downstream section through one of two pneumatic pressure valves. A pressure transducer (PT) provides the signal for the acting pressure control loops. The simplified control loops are indicated with dashed lines. Manually operated purge valves are used during startup and shutdown.
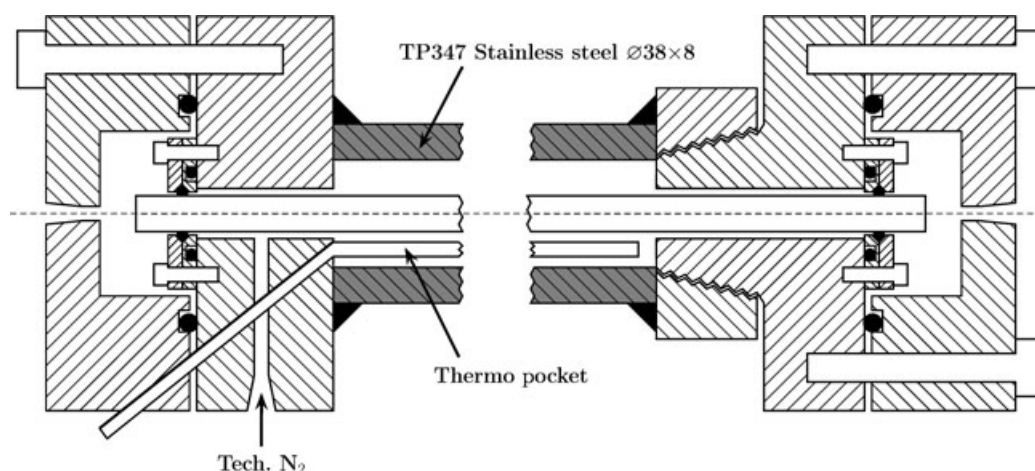
Figure 3 Principle design of the two AISI 316 stainless steel flanges (light hatched parts) with the two small AISI 316 steel plates and the tubular quartz reactor mounted inside. Positions of bolts are indicated by white silhouettes. Gray hatched parts illustrate the TP347 stainless steel pressure shell. Black circles are Viton O-rings, and black triangles indicate welded connections.

incorporated in one of the flanges and so is the access to the two steel thermo-pockets that contain the thermo-couples in the space between the reactor and the steel shell. The thermo-pockets are sealed from any contact with the high-pressure area by welding. The flanges are bolted together using a third Viton O-ring to seal the high pressure inside. The bolts are easily removed to gain access to the reactor tube or the Viton O-rings in case they need to be changed.

Experimental data are obtained as mole fractions as a function of the reactor temperature measured at intervals of typically 25 K. Hence, each measurement represents the steady-state concentration at a constant temperature, pressure, and flow rate. This makes the residence time τ throughout an experimental series depend solely on the temperature in accordance with

$$\tau = \frac{V}{F[\text{m}^3/\text{s}]}$$

$$= \frac{\pi}{4} D^2 L_{\text{iso}} \left(F[\text{Nm}^3/\text{s}] \frac{T}{273.15\text{K}} \frac{1\text{bar}}{P} \right)^{-1} \quad (1)$$

where V is the volume of the isothermal reaction zone. D is the inner diameter of the reactor tube, and L_{iso} is the isothermal length (± 3 cm) as determined below. The volumetric flow rate $F(\pm 2\%)$ is measured during experiments in units of "normal" cubic meters per second (Nm^3/s). Conversion to m^3/s is based on the application of the ideal gas law, which has been verified at the current high-pressure conditions by calculations of compressibility factors (Z) for representative gas mixtures of N$_2$, O$_2$, H$_2$, H$_2$O, CO, CO$_2$, CH$_4$, and

CH$_3$OH, using the Peng–Robinson cubic equation of state [25] with customary mixing rules based on a random mixing approximation [26]. Calculations at high pressure from 10 to 100 bar and medium temperatures from 600–900 K, which encompass the typical operational range of the system, yield maximum deviations of Z from unity of 4%. This result validates the ideal gas assumption.

Calculations indicate that the reactor operates in the laminar flow regime with a steady, fully developed laminar flow profile. Hence, $75 < Re < 564$ for representative gas mixtures within the operational range of the system. The flow pattern has been confirmed by a CFD calculation (Fluent 6.2, Fluent Inc.), which has also verified that potential vertical upward components of the velocity profile as a result of natural convection following the horizontal positioning of the reactor are negligible.

It is reasonable to approximate the laminar flow field to plug flow and reduce the mathematical description from a 2D to a 1D problem if the gas is premixed and the radial velocity gradients are sufficiently small to allow fluid elements to exhibit similar residence times. The former is readily obtained in the present setup due to a very long mixing section before the reactor inlet. A useful measure of the radial velocity gradients in laminar flow is the longitudinal or axial dispersion [27,28] that characterizes the spreading, or overtaking, of fluid elements as a result of different local flow velocities and molecular diffusion. This process is represented by the dispersion coefficient $D_{\text{disp}}(=\text{m}^2/\text{s})$, where large values of D_{disp} indicate rapid spreading and hence, mixed flow, whereas lower values indicate

slower spreading until $D_{\text{disp}} = 0$ that corresponds to ideal plug flow. The numeric value of D_{disp} can be determined either from flow experiments with a single injection of a trace species at the inlet and subsequent measurement of the outlet concentration or from the correlation

$$D_{\text{disp}} = \mathscr{D}_{AB} + \frac{u^2 D^2}{192 \mathscr{D}_{AB}} \qquad (2)$$

from Levenspiel [27,28] that was derived from the early work of Taylor [29] and Aris [30]. This correlation illustrates that the dispersion coefficient depends strongly on the molecular diffusion $\mathscr{D}_{AB}$. It promotes dispersion at low linear flow rates u, while it has an opposite effect at high flow rates, where dispersion is instead facilitated by axial convection with radial diffusion. Consequently, there is an optimum relation between values of $\mathscr{D}_{AB}$, and u and D in terms of low axial dispersion; here expressed by the dimensionless group D_{disp}/uD. If the reactor length L is chosen as characteristic length instead of the diameter D, the dimensionless group can be referred to as the *vessel dispersion number* that exhibits an upper critical limit of 0.01 to delimit "small" deviations from plug flow

[27,28]. The ratio between mass transfer by convection and diffusion is expressed by the Peclet number (also known as the Bodenstein number, Bo), which is the product of the Reynolds' and the Schmidt numbers:

$$Pe = Re \times Sc = \frac{\rho u D}{\mu} \frac{\mu}{\rho \mathscr{D}_{AB}} = \frac{uD}{\mathscr{D}_{AB}} \qquad (3)$$

Figure 4 correlates D_{disp}/uD with Pe (shown as Bo) for steady laminar pipe flow, modified from Levenspiel [28]. The bottom of the curve defines the optimum conditions for low axial dispersion in laminar pipe flow, and hence, the conditions where the plug flow assumption is most accurate. Considering representative gas mixtures at temperatures from 600–900 K and 10–100 bar, calculations of D_{disp}/uD and Pe have been conducted at volumetric flow rates from 1 to 5 NL/min and the resulting function value span depicted in Fig. 4.

Even though this approach does not account for differences in diffusion coefficients between species and a representative value has to be chosen, it provides a useful measure of the plug-flow approximation. The highlighted intervals of D_{disp}/uD and Pe in Fig. 4 reveal that optimum conditions in terms of low axial dispersion are nearly obtained at the lowest possible flow
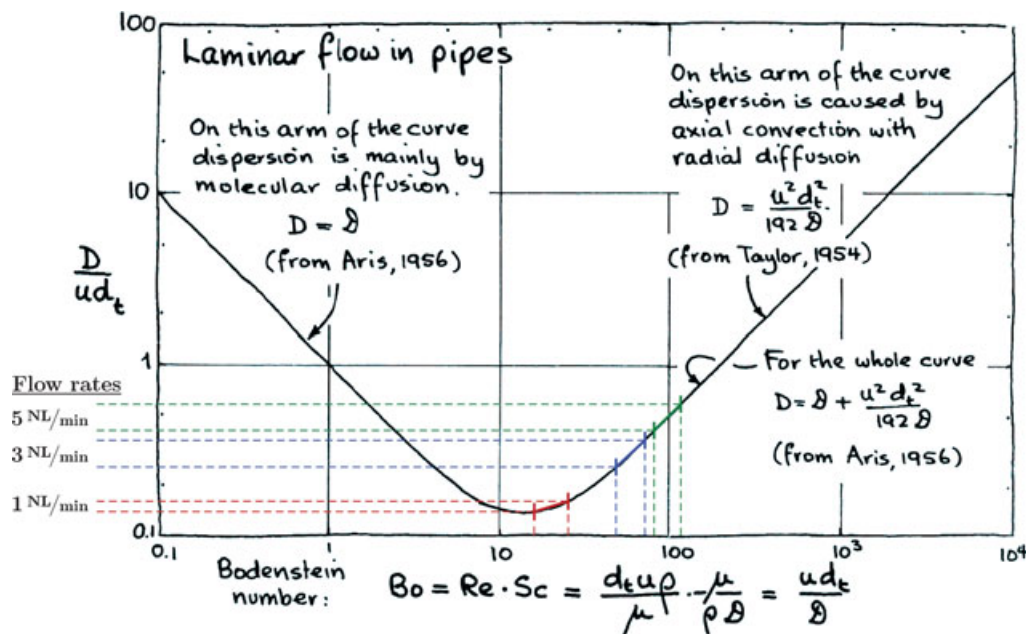
Figure 4 Intensity of axial dispersion (D_{disp}/uD) correlated with the Peclet number, Pe (here denoted the Bodenstein number, Bo). The bottom of the curve ($D_{\text{disp}}/uD = 0.14$ and $Pe = 13$) defines the optimum conditions for low axial dispersion in steady laminar pipe flow, and hence, the desired conditions where the plug flow assumption is most accurate. Marked line segments denote ranges of D_{disp}/uD and Pe obtained for representative gas mixtures within the operational range of the system (see text). Results are given for the specific volumetric flow rates of 1, 3, and 5 NL/min. The figure is courtesy of Octave Levenspiel [28]. Here, "D" denotes the dispersion coefficient (D_{disp}), whereas "d_t" is the diameter of the flow cross section (D in the present work). [Color figure can be viewed in the online issue, which is available at www.interscience.wiley.com.]

rate of the system (1 NL/min) indicating a good plug flow assumption. Plug flow may, on the other hand, be a questionable assumption when the system is operated at the highest volumetric flow rate of 5 NL/min. Moreover, the relatively high values of Pe indicate that dispersion is generally caused by axial convection rather than molecular diffusion. In the present work, all experiments have been conducted with a volumetric flow rate of 3 NL/min under which conditions, it is still reasonable to assume plug flow. The latter issue is verified by further calculations of the vessel dispersion number D_{disp}/uL_{iso} for this specific volumetric flow rate. It yields values of $0.005 < D_{disp}/uL_{iso} < 0.007$, which is below the critical limit of 0.01.

DETAILED KINETIC MODEL

Ranging from low-temperature conditions, relevant to atmospheric chemistry, to the high temperatures obtained in typical combustion systems, the kinetic mechanism roughly falls into two regimes that are highly diverse in nature. At low temperatures, the kinetic scheme is operated by seemingly slow chain-propagating reactions controlled by HO$_2$ radicals and intermediate H$_2$O$_2$ formation, whereas high temperatures facilitate a fast chain-branching regime operated by a radical pool dominated by the very reactive O, H, and OH radicals. The primary operational range of the present kinetic model is roughly temperatures from 500 to 1100 K and pressures from atmospheric to 100 bar. This range encompasses the transition between these two kinetic regimes. Consequently, it is relevant to revisit the important reaction subsets with special attention to pressure-dependent reactions and intermediate temperature evaluations of rate constants, and to draw upon previous experience from both low- and high-temperature investigations.

The proposed reaction mechanism consists of a description of the H$_2$/O$_2$ system as well as subsets describing reactions involving CO/CO$_2$ and NO$_x$, respectively. Table I contains thermodynamic properties: enthalpies of formation, entropies, and specific heats for the species included in the model. Data are drawn from the Thermochemical Database of Burcat and Ruscic [31] and include the latest evaluation of enthalpies of formation from the Active Thermochemical Tables of Ruscic et al. [32,33]. Data for HOCO are adopted from recent ab initio calculations by Fabian and Janoschek [34] and fitted to seven-constant NASA polynomials.

H$_2$/O$_2$ Subset

The H$_2$/O$_2$ reaction mechanism is important in a number of fields related to energy conversion and propulsion, and it plays a key role in fundamental chemical

Table I Thermodynamic Properties of Species Included in the Reaction Mechanism

Species	$\Delta H_{f,298}$	S_{298}	$C_{p,400}$	$C_{p,600}$	$C_{p,800}$	$C_{p,1000}$	$C_{p,1500}$	Reference
H	52.10	27.42	4.97	4.97	4.97	4.97	4.97	[31]
H$_2$	0.0	31.23	7.00	6.99	7.08	7.21	7.73	[31]
O	59.55	38.49	5.13	5.05	5.02	5.00	4.98	[31]
O$_2$	0.0	49.03	7.20	7.67	8.07	8.34	8.72	[31]
OH	8.92	43.91	7.07	7.06	7.15	7.34	7.88	[31,33]
H$_2$O	−57.79	45.13	8.19	8.68	9.26	9.87	11.31	[31]
HO$_2$	2.94	54.75	8.89	9.99	10.77	11.38	12.48	[31,33]
H$_2$O$_2$	−32.43	56.05	11.09	12.79	13.99	14.95	16.59	[31,33]
CO	−26.41	47.24	7.02	7.27	7.62	7.93	8.40	[31]
CO$_2$	−94.04	51.09	9.86	11.32	12.29	12.98	13.91	[31]
HOCO	−44.33	60.07	12.01	14.04	15.35	16.27	17.70	[34]
HCO	10.11	53.60	8.75	9.84	10.85	11.66	12.94	[31]
CH$_2$O	−25.95	52.28	9.36	11.52	13.37	14.82	16.93	[31]
NO	21.76	50.36	7.16	7.46	7.83	8.12	8.54	[31,33]
NO$_2$	8.13	57.40	9.67	11.09	12.05	12.67	13.43	[31,33]
NO$_3$	17.83	60.37	13.28	16.16	17.51	18.31	19.09	[31]
N$_2$O$_3$	20.56	75.22	18.57	20.36	21.72	22.58	23.64	[31]
N$_2$O$_4$	2.58	72.76	21.63	25.20	27.21	28.36	29.57	[31]
HNO	25.52	52.80	8.48	9.54	10.56	11.40	13.28	[31]
HONO	−18.74	60.72	12.41	14.43	15.69	16.58	17.88	[31]
HNO$_2$	−9.80	56.73	10.40	12.71	14.47	15.77	17.56	This study
HONO$_2$	−32.03	63.76	15.32	18.73	20.72	21.96	23.34	[31]

Units are kcal/mol for H and cal/(mol K) for S and C_p.

Table II   Reactions from the Hydrogen/Oxygen Subset

	Reactions	A	β	E	Note/Reference
1.	$H + H + M \rightleftharpoons H_2 + M^a$	7.00×10^{17}	-1.0	0	[46,168]
	$H + H + H_2 \rightleftharpoons H_2 + H_2$	1.00×10^{17}	-0.6	0	[46,168]
	$H + H + N_2 \rightleftharpoons H_2 + N_2$	5.40×10^{18}	-1.3	0	[46,168]
2.	$H + O + M \rightleftharpoons OH + M^b$	6.20×10^{16}	-0.6	0	[104]
3.	$H + O_2 \rightleftharpoons O + OH$	3.55×10^{15}	-0.41	16600	[36,37]
4.	$H + O_2(+M) \rightleftharpoons HO_2(+M^c)$	1.48×10^{12}	0.6	0	[39]
	Low-pressure limit:	3.50×10^{16}	-0.41	-1116	[36]
	Troe parameters: 0.5 10^{-30} 10^{30} 10^{30}				
	$H + O_2(+Ar) \rightleftharpoons HO_2(+Ar)$	1.48×10^{12}	0.6	0	[39]
	Low-pressure limit:	9.04×10^{19}	-1.5	490	[36,40]
	Troe parameters: 0.5 10^{-30} 10^{30} 10^{30}				
	$H + O_2(+N_2) \rightleftharpoons HO_2(+N_2)$	1.48×10^{12}	0.6	0	[39]
	Low-pressure limit:	6.37×10^{20}	-1.72	520	[36,40]
	Troe parameters: 0.8 10^{-30} 10^{30} 10^{30}				
5.	$O + O + M \rightleftharpoons O_2 + M^d$	1.89×10^{13}	0.0	-1788	[46]
6.[e]	$O + H_2 \rightleftharpoons OH + H$	3.82×10^{12}	0.0	7950	[41]
		8.79×10^{14}	0.0	19170	
7.	$OH + OH \rightleftharpoons O + H_2O$	4.33×10^{3}	2.7	-1822	[42,43]
8.	$OH + H + M \rightleftharpoons H_2O + M^f$	4.50×10^{22}	-2.0	0	[35,46]
9.	$OH + H_2 \rightleftharpoons H + H_2O$	2.14×10^{8}	1.52	3450	[42]
10.	$H_2 + O_2 \rightleftharpoons HO_2 + H$	7.40×10^{5}	2.433	53500	[50]
11.	$HO_2 + H \rightleftharpoons OH + OH$	8.40×10^{13}	0.0	400	See text
12.	$HO_2 + H \rightleftharpoons H_2O + O$	1.40×10^{12}	0.0	0	[41]
13.	$HO_2 + O \rightleftharpoons OH + O_2$	1.63×10^{13}	0.0	-445	[41]
14.[e]	$HO_2 + OH \rightleftharpoons H_2O + O_2$	3.60×10^{21}	-2.1	9000	See text
		2.00×10^{15}	-0.6	0	
		-2.20×10^{96}	-24.0	49000	
15.[e]	$HO_2 + HO_2 \rightleftharpoons H_2O_2 + O_2$	1.94×10^{11}	0.0	-1408	[65]
		1.03×10^{14}	0.0	11034	
16.	$H_2O_2(+M) \rightleftharpoons OH + OH(+M^g)$	4.00×10^{11}	0.0	37137	[65]
	Low-pressure limit:	2.29×10^{16}	0.0	43640	
	Troe parameters: 0.5 10^{-30} 10^{30} 10^{30}				
17.	$H_2O_2 + H \rightleftharpoons HO_2 + H_2$	1.69×10^{12}	0.0	3760	[41]
18.	$H_2O_2 + H \rightleftharpoons H_2O + OH$	1.02×10^{13}	0.0	3580	[41]
19.	$H_2O_2 + O \rightleftharpoons HO_2 + OH$	9.55×10^{6}	2.0	3970	[46]
20.[e]	$H_2O_2 + OH \rightleftharpoons H_2O + HO_2$	1.93×10^{12}	0.0	427	[64]
		1.64×10^{18}	0.0	29410	

Units are mol, cm, s, cal.

[a] Enhanced third-body efficiencies: $N_2 = 0$, $H_2 = 0$, $H_2O = 14.3$.

[b] Enhanced third-body efficiencies: $H_2O = 5$.

[c] Enhanced third-body efficiencies: $N_2 = 0$, $Ar = 0$, $H_2 = 2$, $O_2 = 0.78$, $H_2O = 11$.

[d] Enhanced third-body efficiencies: $N_2 = 1.5$, $O_2 = 1.5$, $H_2O = 10$.

[e] Expressed as the sum of the rate constants.

[f] Enhanced third-body efficiencies: $Ar = 0.38$, $H_2 = 0.73$, $H_2O = 12$.

[g] Enhanced third-body efficiencies: $Ar = 0.64$, $H_2 = 2.5$, $H_2O = 12$.

kinetic research where the elementary reactions of H, O, OH, HO_2, and H_2O_2 govern the composition of the radical pool in hydrocarbon reaction systems. Comprehensive modeling studies have been conducted in this field; and recent examples [1,35,36] are based on numerous individual reaction rate measurements and theoretical estimates. Nevertheless, some details remain unsettled. The proposed H_2/O_2 reaction subset is shown in Table II.

Interaction with O_2 and the radical pool is largely governed by H atom consumption via the branching reaction (R3) to form O—OH or the competing reaction (R4) yielding collisionally stabilized HO_2 radicals. HO_2 is far less reactive than H causing an inhibition of the overall reaction rate when (R4) dominates. The ratio R3/R4 thus becomes a decisive parameter when determining whether the overall governing reaction mechanism is mainly chain branching (fast) or chain

propagating (slow) in nature. Reactions (R3) and (R4) have recently been subjected to thorough revision by Li et al. [36]. Following their recommendations, reaction (R3) is drawn from the work of Hessler [37]. This is in excellent agreement with more recent shock tube experiments by Hwang et al. [38] at 950–3100 K. Reaction (R4) is represented by the high-pressure limit from Cobos et al. [39] and the newly fitted low-pressure limits from Li et al. [36] based on experimental data from Michael et al. [40] using different bath gases and corresponding Troe parameters to describe the falloff region. High values of R3/R4 facilitate a significant O radical pool, which further promotes the chain-branching reaction O + H$_2$ ⇌ OH+H (R6). This reaction is well characterized by numerous experimental measurements and literature evaluations at temperatures from 300–2500 K. The applied rate from Baulch et al. [41] matches these data across the entire temperature range.

H$_2$ is mainly oxidized by reaction with OH radicals (R9). This is an important H$_2$O formation reaction, and the rate expression is well established from multiple experimental measurements [42,41]. Other H$_2$O formation channels are the radical termination reactions OH+OH (R7) and OH+H+M (R8). The rate constant for (R7) originates from the transition state calculations by Michael [42] at temperatures from 700 to 2500 K with a minor recent update by Srinivasan and Michael [43] using the latest OH heat of formation. The rate constant is in excellent agreement with the high-temperature flash photolysis-shock tube measurements by Lifshitz and Michael [44] (1500–2400 K) and Sutherland et al. [45] (1053–2023 K). (R8) is adopted from the hydrogen oxidation modeling study of O'Conaire et al. [35], where the recommended value of Tsang and Hampson [46] was increased by a factor of 2 to improve the prediction of experimental data from a wide range of conditions and experimental facilities. This revision is well within the uncertainty limits of existing evaluations of (R8) [35].

The mechanism includes three competitive product channels from the reaction between HO$_2$ and H yielding the stable products H$_2$+O$_2$ (–R10), two OH radicals (R11), and H$_2$O+O (R12), respectively. In the forward direction, (R10) constitutes the primary initiation reaction of H$_2$/O$_2$ mixtures. Valid rate data for HO$_2$+H are limited to a few room-temperature measurements [47,48], an experimental/modeling study of the second pressure limit of explosion of H$_2$/O$_2$ in boric acid coated vessels at 773 K [49], and recent shock tube measurements of H$_2$+O$_2$ by Michael et al. [50] at high temperatures (1662–2097 K). Michael et al. combined their measurements with the low-temperature data from [47,48] and ab initio calculations to derive the rate constant for (R10) applied in Table II, which

covers the temperature range 400–2300 K. Baldwin et al. [49] expressed rate constant data as optimized values for $k_{-10}/k_3 k_{15}^{1/2}$ and $k_{11}/k_3 k_{15}^{1/2}$ at 773 K. Following the approach of Mueller et al. [1], the value of the latter parameter has been updated by incorporating the rate constants of (R3) and (R15) from Table II to yield a value of k_{11} at 773 K. This value is combined with the room-temperature measurements from Sridharan et al. [47] and Keyser [48] to yield an expression of $k_{11} = 8.4 \times 10^{13} \exp(-400/RT) cm^3/mol$ s). This value is almost identical to the recommendation by Mueller et al. [1] at room temperature, but increases slightly faster with temperature. The obtained branching ratio $k_{11}/(k_{-10} + k_{11} + k_{12}) = 89\%$ at room temperature is in excellent agreement with recommendations from both Sridharan et al. and Keyser. The ratio decreases to 87% and 65% at 773 and 2000 K, respectively. The third product channel to H$_2$O+O (R12) is included in the model despite experimental indications of a low contribution [47,48]. k_{12} is taken from the recent review by Baulch et al. [41] and yields $k_{12}/(k_{-10} + k_{11} + k_{12})$ <3% below 2000 K, consistent with [47,48].

The reaction of HO$_2$ with O (R13) only has one possible product channel leading to OH+O$_2$. The reaction plays an important role in the degeneration of HO$_2$ radicals in the upper atmosphere, which has encouraged a number of experimental rate measurements at low temperatures (229–391 K), e.g. [51,47,52]. These indicate a slightly negative temperature dependence. High-temperature measurements are sparse and subjected to significant uncertainties and, hence, provide no conclusive indications of the temperature dependence in this range. The present mechanism applies the recent recommendation by Baulch et al. [41], which includes a negative temperature dependence matching the available low-temperature measurements.

The reactions of HO$_2$ with H and O compete with the important OH radical termination step HO$_2$+OH ⇌ H$_2$O+O$_2$ (R14). This reaction deserves special attention due to a strong non-Arrhenius temperature dependence at conditions relevant to this study. Figure 5 shows experimental measurements [53–66] and comparisons with recently recommended rate expressions [18,41] as well as a novel fit by the authors (full line). Reaction (R14) plays an important role in the conversion of HO$_2$ and OH in the upper atmosphere and, as a consequence, numerous studies have been conducted at low temperatures from 231 to 420 K [55–61]. These findings fall into two groups with rate constants between $(2–5) \times 10^{13}$ and $(6–8) \times 10^{13}$ cm^3(mol s), respectively; all indicating a negative temperature dependence; see Fig. 5. Keyser [61] suggested that the systematic discrepancy between the measurements of these two groups was a result of secondary reactions
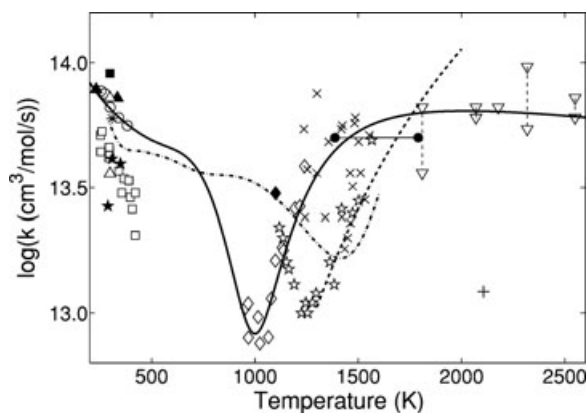
Figure 5 Rate constant of reaction (R14) as a function of temperature. + Friswell and Sutton [53]; ⊶ Peeters and Mahnen [54]; ▲DeMore [55]; ★Burrows et al. [56]; ∗ Cox et al. [57] ■ Kurylo et al. [58]; △ DeMore [59]; □ Sridharan et al. [60]; ○ Keyser [61]; ▽--▽ Gooding and Hayhurst [62]; ◆ Hippler et al. [63]; ☆ Hippler et al. [64]; ◇ Kappel et al. [65]; × Srinivasan et al. [66]; - - Baulch et al. [41]; –•– Sivaramakrishnan et al. [18]; — This work.

with H and O causing a lower rate constant determination by Sridharan et al. [60] and others. Keyser avoided this interference by addition of NO_2 to remove H and O radicals. Keyser also noticed that the reaction showed little or no pressure dependence below 1.3 bar across the investigated temperature range. Subsequent literature evaluations [41,67,68] have adopted the rate expression proposed by Keyser in the low-temperature region. However, this rate constant does not reproduce the available high-temperature data [53,54,62–66]. Hippler et al. [64] conducted shock tube measurements of the thermal decomposition of H_2O_2 and located the deep and unusually narrow rate constant minimum at 1250 K. In a more recent study from the same group, Kappel et al. [65] confirmed this behavior, but this time the rate constant minimum was located at about 1000 K. Kappel et al. measured reactant concentrations more accurately than Hippler et al. and reduced the uncertainty of the rate derivation considerably. As a consequence, more confidence is placed in the later results from Kappel et al. At high temperatures from 1300 to 2300 K, temperature independent rate constants of about $(4-6)\times10^{13}$ cm^3/(mol s) have been determined by Peeters and Mahnen [54], Gooding and Hayhurst [62] and, most recently, by Srinivasan et al. [66], even though the latter results show considerable scatter. The proposed fit by the authors reproduces the low-temperature data of Keyser [61] as well as the high-temperature data [54,62,66], while the intermediate temperature region, including

the characteristic rate constant minimum, is matched to the measurements reported by Kappel et al. [65]. The authors note that the proposed rate expression needs validation in the range 400–950 K, but this is impossible at the moment due to insufficient experimental data.

The self-reaction of HO_2 to $H_2O_2+O_2$ (R15) and subsequent decomposition of H_2O_2 to OH via (R16) is the main conversion path of H_2O_2. The reaction rates are adopted from Kappel et al. [65] including falloff curves for the decomposition reaction. Kappel et al. did not observe any pressure dependence of (R15) in the investigated temperature range 950–1250 K. Other possible H_2O_2 consumption channels are radical reactions with H (R17), (R18), O (R19), and OH (R20). The reaction with H is analogous to HO_2+H with two product channels yielding H_2O+OH and HO_2+H_2. The present mechanism involves the rate coefficients recommended by Baulch et al. [41], which result in an almost constant branching ratio $k_{17}/(k_{17}+k_{18})$ close to 90%. These recommendations are based on available experimental data [69–71] obtained at 300–1000 K. It is noted that Baulch et al. apply a significantly lower positive temperature dependence than, e.g. Tsang and Hampson [46]. However, both studies assign large uncertainty margins to the recommended rate coefficients; mainly due to possible unquantified effects from secondary reactions during the experimental work. H_2O_2+O has two principle product channels that are chain branching and terminating in nature yielding HO_2+OH (R19) and H_2O+O_2, respectively. Experimental investigations of the product branching ratio $k_{19}/(k_{H_2O_2+O})$ are highly uncertain indicating values from >0.2 [72] to unity [73]. In the present study, k_{19} is set equal to the overall rate of H_2O_2+O as recommended by Tsang and Hampson [46].

The biexponential rate constant for H_2O_2+OH (R20) is drawn from Hippler et al. [64], who combined new and previous [63,74] shock tube measurements across an overall temperature range of 930–1680 K with available low and intermediate temperature results from the literature, e.g., [75–77]. The rate constant shows a weak positive temperature dependence up to ~800 K followed by a marked change in the activation energy and a substantial increase of the rate constant until the reaction again levels off at temperatures >1600 K. Hippler et al. [64] attributed this behavior to intermediate complex formation and subsequent competition between forward and backward dissociation pathways. It is noted that the current rate constant does not account for the apparent constant-temperature behavior of the rate constant observed by Hippler et al. [64] at >1600 K.

Table III Reactions from the CO/CO$_2$ Subset

	Reactions	A	β	E	Note/Reference
21.	CO + O(+M) $\rightleftharpoons$ CO$_2$(+M^a)	1.80×10^{10}	0.0	2384	[107,169]
	Low-pressure limit:	1.35×10^{24}	-2.79	4191	[107,170]
	Troe parameters: 1.0 10^{-30} 10^{30} 10^{30}				
22.	CO + O$_2$ $\rightleftharpoons$ CO$_2$ + O	4.70×10^{12}	0.0	60500	[92]
23.	CO + HO$_2$ $\rightleftharpoons$ CO$_2$ + OH	1.57×10^{5}	2.18	17940	[100]
24.^{b}	CO + OH $\rightleftharpoons$ CO$_2$ + H	8.00×10^{10}	0.0	0	See text, 1 bar
		8.80×10^{5}	1.77	954	1 bar
	CO + OH $\rightleftharpoons$ CO$_2$ + H	3.70×10^{12}	0.0	12518	10 bar
		9.30×10^{7}	1.1	0	10 bar
	CO + OH $\rightleftharpoons$ CO$_2$ + H	2.90×10^{12}	0.0	11922	20 bar
		4.50×10^{7}	1.2	0	20 bar
	CO + OH $\rightleftharpoons$ CO$_2$ + H	1.50×10^{12}	0.0	13909	50 bar
		5.80×10^{6}	1.5	0	50 bar
	CO + OH $\rightleftharpoons$ CO$_2$ + H	1.50×10^{11}	0.0	1987	100 bar
		1.87×10^{5}	1.94	0	100 bar
25.^{b}	CO + OH $\rightleftharpoons$ HOCO	2.00×10^{26}	-5.6	2881	See text, 1 bar
	CO + OH $\rightleftharpoons$ HOCO	1.50×10^{25}	-5.0	1987	10 bar
		1.30×10^{37}	-8.4	7948	10 bar
	CO + OH $\rightleftharpoons$ HOCO	4.20×10^{26}	-5.7	1927	20 bar
		7.50×10^{28}	-6.0	3775	20 bar
		4.00×10^{39}	-9.0	9935	20 bar
	CO + OH $\rightleftharpoons$ HOCO	4.90×10^{25}	-5.2	1987	50 bar
		4.00×10^{38}	-9.0	6955	50 bar
		5.00×10^{43}	-10.0	13015	50 bar
	CO + OH $\rightleftharpoons$ HOCO	1.10×10^{28}	-6.0	2384	100 bar
		1.84×10^{36}	-8.0	7153	100 bar
		2.00×10^{54}	-13.0	19671	100 bar
26.^{c}	HOCO $\rightleftharpoons$ CO$_2$ + H	P[bar]$^{0.95} \times 3.50 \times 10^{56}$	-15.0	46500	See text
		P[bar]$^{0.95} \times 2.50 \times 10^{69}$	-18.0	60000	
27.^{c}	HOCO + OH $\rightleftharpoons$ CO$_2$ + H$_2$O	4.56×10^{12}	0.0	-89	[101]
	HOCO + OH $\rightleftharpoons$ CO$_2$ + H$_2$O	9.54×10^{6}	2.0	-89	
28.	HOCO + OH $\rightleftharpoons$ CO + H$_2$O$_2$	1.00×10^{13}	0.0	0	Est
29.	HOCO + O$_2$ $\rightleftharpoons$ CO$_2$ + HO$_2$	9.91×10^{11}	0.0	0	[102]

Units are mol, cm, s, cal.

^{a} Enhanced third-body efficiencies: H$_2$ = 2.5, H$_2$O = 12, CO = 1.9, CO$_2$ = 3.8.

^{b} Expressed as the sum of the rate constants at a given pressure.

^{c} Expressed as the sum of the rate constants.

CO/CO$_2$ Subset

The carbon subset (Table III) describes the conversion of CO to CO$_2$. To account for a potential minor flux toward the oxygenated hydrocarbon species formyl (HCO) and formaldehyde (CH$_2$O) facilitated by the high pressure, the mechanism also contains a simple HCO/CH$_2$O reaction subset.

Oxidation of CO by OH is the most important reaction in the subset. In hydrocarbon combustion, this reaction is responsible for a major fraction of the heat release. The reaction further regulates the OH radical concentration, which plays a decisive role in HO$_x$ and NO$_x$ cycles that are important in both combustion and atmospheric chemistry research. The reaction of CO+OH presents complex pressure and temperature dependencies with two regimes of markedly different activation energies. At low temperatures, the reaction shows a weakly decreasing temperature dependence, whereas a significant positive temperature dependence is observed at high temperatures. A rate minimum marks the transition, whose characteristics depend on the pressure.

The non-Arrhenius behavior of CO+OH has encouraged numerous experimental and theoretical studies of the reaction across a wide range of conditions, e.g. [78–90]. The accepted mechanism was first proposed by Smith and Zellner [78] and Smith [79]. It involves initial association of the reactants to form the activated *trans*-HOCO* complex followed by

cis–trans isomerization before decomposition to CO_2+H, reaction (R24). The thermal decomposition competes with stabilization of HOCO (R25) and redissociation (−R25). The abnormal change in activation energy can be explained by two important transition states of comparable magnitude located along the reaction coordinate. At low temperatures, energy is insufficient to overcome the second *cis*-HOCO decomposition barrier, allowing the first association transition state to control the overall reaction rate. This favors either stabilization (R25) or redissociation to CO+OH (–R25) depending on the gas density. Once formed, collisionally stabilized HOCO may also decompose to CO_2+H (R26) or it may be converted by other available reactants, like OH (R27,R28) or O_2 (R29). The latter reactions will be discussed later. At high temperatures and/or low pressures, the second transition state controls the overall reaction rate, and the thermal decomposition reaction (R24) predominates. The pressure dependence is related to the overall conversion of CO+OH given by $k_{CO+OH} = k_{24} + k_{25}$. At the high-pressure limit, stabilized HOCO is the sole product as $k_{CO+OH} \to k_{25}$ as $P \to \infty$, while CO_2 and H are the dominating products as the low-pressure limit is approached-yielding $k_{CO+OH} \to k_{24}$ as $P \to 0$. Fulle et al. [83] and Troe [84] developed a complex expression to describe the falloff behavior within these limits. Following this work,

$$k_{24} = k_0 \left[1 - \frac{x}{1+x} F(x) \right]$$

and

$$k_{25} = k_{25,0} \left(\frac{1+y}{1+x} \right) F(x),$$

where $x = k_{25,0}/(k_\infty - k_0)$, $y = k_0/(k_\infty - k_0)$, and k_∞ and k_0 refer to $k_{CO+OH,\infty}$ and $k_{CO+OH,0}$, respectively. The pressure dependence is included in $k_{25,0} = k_0 A_0^* \exp(-T/T^*) P$, where $A_0^* = 5.9 \, \text{bar}^{-1}$ for N_2 as bath gas, and $T^* = 161$ K.

$$F(x) = F_{\text{cent}}^{(1/[1+(\log x)^2])}$$

is the broadening factor with $F_{\text{cent}} = 0.49 + 0.51 \exp(-T/300 \, \text{K})$. Troe [84] proposed values of $k_\infty = [1.23 \times 10^{15}\exp(-7520 \, \text{K}/T) + 1.1 \times 10^{13}\exp(-1850 \, \text{K}/T) + 8.0 \times 10^{11}\exp(-120 \, \text{K}/T)]$ $\text{cm}^3/(\text{mol·s})$ and $k_0 = [1.0 \times 10^{13}\exp(-8050 \, \text{K}/T) + 9.0 \times 10^{11} \exp(-2300 \, \text{K}/T) + 1.01 \times 10^{11} \exp(-30 \, \text{K}/T)]$ $\text{cm}^3/(\text{mol·s})$ to accurately fit experimental data of k_{CO+OH} from [80–83] and others within an extensive temperature range of 80–2370 K and pressures from 0.001–1000 bar. The proposed expression was later recommended in its complete form by [41] based on a comprehensive literature review.

Fulle et al. [83] and Troe [84] estimated the value of $\Delta H^\circ_{298}(\text{HOCO}) = -48.34$ kcal/mol. However, a recent experimental investigation by Ruscic and Litorja [86] determined a lower limit of $\Delta H^\circ_{298}(\text{HOCO}) > -46.5$ kcal/mol, which has later been confirmed by ab initio calculations of the *trans*-HOCO well depth in the CO+OH potential energy surface [34,87,88,91]. The most recent recommendation by Fabian and Janoschek [34] yields a value of $\Delta H^\circ_{298}(\text{HOCO}) = -44.33$ kcal/mol, which is applied in the present study.

The potential energy surface calculations of Yu et al. [88] provided the foundation of another comprehensive investigation of the pressure and temperature dependence of CO+OH kinetics by Senosiain et al. [89,90] using a master equation and RRKM theory. Senosiain et al. proposed new analytical rate expressions of k_{25} and k_{24}, which enabled them to accurately simulate the available experimental data of k_{CO+OH} across the same temperature and pressure range as Troe [84]. However, using the proposed rates of either Troe [84] or Senosiain et al. [89,90] invokes a practical problem, as neither of them are suited for direct implementation in CHEMKIN; or in the case of [90], insufficiently covers the pressure range relevant to this study. As a consequence, the authors have refitted the expression of Troe for k_{CO+OH} using coefficients in a suitable modified Arrhenius form. A comparison with the original expression is shown in Fig. 6 at 300–2000 K and selected pressures. The corresponding modified Arrhenius parameters of k_{25} and k_{24} are provided in Table III. It is of little concern that the original work is based on a too low value of $\Delta H^\circ_{298}(\text{HOCO})$, since the proposed rates by [84] are forward rates derived from experimental data.

Fulle et al. [83] and Troe [84] also provide a rate constant for the dissociation of stabilized HOCO to CO_2+H (R26) based on the equilibrium constant of (R25), $K_{25} = k_{25}/k_{-25}$, and the relation $k_{-25}/k_{26} = k_{CO+OH,\infty}/k_{CO+OH,0} - 1$. Fulle et al. propose a value of $K_{25}(T) = 18.6T^{0.2}\exp(-15680 \, \text{K}/T)\text{mol/cm}^3$ based on their estimated value of $\Delta H^\circ_{298}(\text{HOCO})$. This value is corrected (K'_{25}) in the present study to reflect updated thermodynamic properties of the involved species using the correlation

$$K'_{25}(T) = K_{25}(T) \exp$$
$$\times \left(\frac{\Delta H_{25}(T) - \Delta H'_{25}(T)}{RT} - \frac{\Delta S_{25}(T) - \Delta S'_{25}(T)}{R} \right).$$
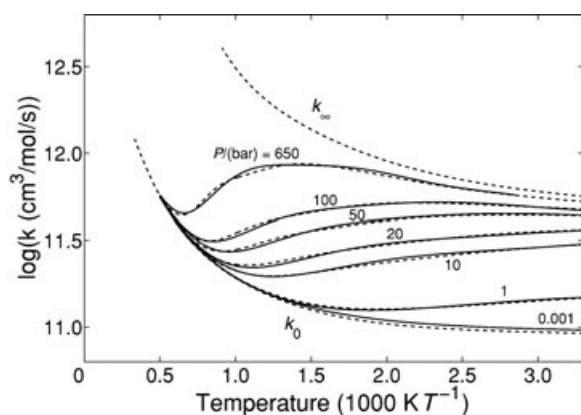
Figure 6 Values of $k_{CO+OH} = k_{24} + k_{25}$ for N$_2$ as bath gas. Dashed lines represent the original rate from [84]. Full lines show the refitted expression in modified Arrhenius form as provided in Table III.

Based on the appropriate values of H and S from Table I to yield $K'_{25}(T)$, and the values of k_{25}, $k_{CO+OH,\infty}$, and $k_{CO+OH,0}$ from [84], k_{26} can be refitted across a temperature and pressure range of 300–2000 K and 1–100 bar. The resulting pressure-dependent expression is $k_{26} = [3.5 \times 10^{56}\ T^{-15}\ \exp(-46500/RT) + 2.5 \times 10^{69}\ T^{-18}\ \exp(-60000/RT)]P^{0.95}$ s^{-1}.

Even though OH is considered the most important reactant to CO, the mechanism also includes reactions of CO with O (R21), O$_2$ (R22), and HO$_2$ (R23). A recent theoretical study of CO + O$_2$ (R22) by Bacskay and Mackie [92] indicates that the rate constant is substantially lower than previously assumed based on experiments [93–96]. Nearly all experimental rate constant determinations rely on shock tube measurements on the CO/H$_2$/O$_2$/Ar system where it is difficult to separate (R22) from the fast oxidation of CO by OH (R24), and, to a lesser extent, the recombination reaction of CO and O (R21). Moreover, Clark et al. [97] have shown that (R22) is readily catalyzed by trace amounts of organic impurities, which may also have influenced a number of the earlier results in the field and given rise to higher rate constants. As a consequence, more confidence is placed in the theoretically based rate constant from Bacskay and Mackie [92].

The rate constant of CO+HO$_2$ (R23) is several orders of magnitude lower than k_{CO+OH}, but it is still of interest in the present study due to the importance of HO$_2$ radicals at high pressure. The reaction has received considerable attention within recent years, e.g. [2,10,18,98–100], but nonetheless, considerable scatter is still observed among experimental as well as theoretical determinations. The preferred rate constant is obtained from the recent theoretical work by You et al. [100] based on ab initio transition state theory with master equation modeling. Calculations of

the potential energy surface for CO+HO$_2$ revealed barrier heights of 17.9 and 18.9 kcal/mol for initial trans- and cis-adduct formation, respectively. Conversion of the energized HOOCO* adduct was examined in terms of hindered internal rotations and relevant transition states, which demonstrated that stabilization of HOOCO is negligible and the reaction can be considered independent of pressure up to 500 bar at 300–2500 K using $k_{23} = 1.6 \times 10^5 T^{2.18} \exp(-9030/T)$ cm^3/(mol s). You et al. [100] emphasized a substantial uncertainty factor for the low-temperature range of this rate expression yielding a value of 8 at 300 K, but at above 1000 K, the uncertainty factor had decreased below a value of 2. Despite these error limits, almost all previous rate constant determinations fall outside the prediction range of You et al. The only exception are data from recent autoignition experiments by Mittal et al. [98] at 950–1100 K that were predicted within 10% accuracy. Limited support is also found in the ab initio study by Sun et al. [99] from which, the predicted rate constant is larger than the preferred value by a factor of 2.5–1.7 at temperatures ranging from 300 to 2000 K. Prior experimentally based proposals of the rate constant, e.g. by Tsang and Hampson [46] and Mueller et al. [2], lie significantly higher.

Only few reports are available concerning bimolecular reactions with HOCO. The present model only considers the reactions with OH and molecular oxygen. The former has two product channels leading to CO$_2$+H$_2$O (R27) and CO+H$_2$O$_2$ (R28), while reaction with O$_2$ yields CO$_2$+HO$_2$ (R29). There are no experimental measurements of HOCO+OH, but a theoretical study at temperatures from 250 to 800 K was recently published by Yu et al. [101] showing that the reaction is essentially barrierless and exhibits a high rate constant ranging from 6.2×10^{12} to 1.1×10^{13} cm^3/(mol s) across the investigated temperature range. However, Yu et al. did not consider the competing pathway to CO+H$_2$O$_2$ (R28). This channel is mainly interesting in the reverse direction (–R28) because it offers a direct reaction path for the stable compounds CO and H$_2$O$_2$ that may gain importance under low-temperature combustion of CO/H$_2$ mixtures. Preliminary scans along the singlet surface for HOCO+OH $\rightarrow$ CO+H$_2$O$_2$ at the B3LYP/6-31G(d) level of theory did not reveal any barrier to this exothermic process. However, this initial computational result must be treated cautiously as multireference methods may be more appropriate at large radical–radical separations. At present, the model applies an estimated temperature independent rate constant of $k_{28} = 1 \times 10^{13}$ cm^3/(mol s). A more thorough investigation is desirable for the HOCO+OH reaction.

The rate constant of HOCO+O$_2$ (R29) is taken directly from the room-temperature measurement of

Nolte et al. [102], which is in good agreement with the only other available experiments by Petty et al. [103], also conducted at room temperature.

NO_x Subset

The presence of NO_x influences the oxidation of CO/H_2 through interactions with the radical pool as well as direct reactions between NO_x and stable species; in particular H_2 and O_2. A number of reactions take place that recycle NO and NO_2 directly or through intermediate formation and subsequent decomposition of nitrous acid (HONO), most importantly $NO+O(+M) \leftrightharpoons NO_2(+M)$ (R31), $NO+O_2 \leftrightharpoons NO_2+O$ (−R37), $NO_2+H \leftrightharpoons NO+OH$ (R34), $NO+HO_2 \leftrightharpoons NO_2+OH$ (R33), $NO_2+HO_2 \leftrightharpoons HONO+O_2$ (R40), and HONO $(+M) \leftrightharpoons NO+OH(+M)$ (−R32). These NO_x cycling reactions have received significant attention, and a large body of experimental and theoretical investigations are available in the field as well as a number of comprehensive kinetic models, e.g. [2,104–108].

The nitrogen reaction mechanism is provided in Table IV. Some of these reactions only play secondary roles under the conditions of interest, and hence, will not be discussed in detail. It is noted that compounds like N_2O and N_xH_y are not included in the mechanism, since these are only formed from NO_x at temperatures beyond those relevant to this study. Relevant subsets can, however, be obtained from the literature, e.g. [107,109–111] in order to extend the operational temperature range of the present mechanism.

Of particular interest has been the role of HNO_2, a thermodynamically less stable isomer of HONO. Its existence has been verified experimentally by Koch and Sodeau [112] from photochemistry experiments with $HONO_2$ in a cryogenic environment (4.2 K), but even so, the compound is rarely considered in combustion modeling. The HNO_2 isomer is potentially important because it does not decompose to OH radicals like HONO. Instead, it may act as a OH radical sink through $HNO_2+OH \leftrightharpoons NO_2+H_2O$ (R63), and consequently, inhibit the overall fuel conversion rate. This effect will, however, be diminished if isomerization to HONO (R61) is sufficiently fast.

The enthalpy of formation of HNO_2 was assessed in the present work via the CBS-QB3 $\Delta_r H_{298}$ for the isodesmic process

$$HNO + NO_2 \rightarrow HNO_2 + NO$$
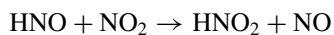
together with the data in Table I to yield $\Delta_f H_{298}(HNO_2) = -9.80$ kcal/mol. This compares well with prior calculations of -8.5 ± 2 kcal/mol by

Nguyen et al. [113] and −10.9 kcal/mol by Asatryan et al. [114]. The B3LYP/6-311G(d,p) moments of inertia and frequencies (scaled by 0.99) were employed to derive the entropy and heat capacities listed in Table I. Important formation pathways for HNO_2, such as NO_2+HO_2 and NO_2+H_2, are discussed in detail below. Regarding consumption of HNO_2, ab initio calculations indicate that the transition state for HNO_2+OH lies well below the level of the reactants, which means that the reaction is, essentially, barrierless with a high-rate constant of $k_{63} \approx 4 \times 10^{13}$ cm^3/(mol s) at 600–1200 K. The calculated CBS-QB3 barriers to isomerization (R61) were 47.3 and 55.3 kcal/mol relative to HNO_2 and HONO, respectively. These are consistent with previous ab initio results from Chan et al. [115] that indicated an isomerization barrier between HNO_2 and HONO in excess of 50 kcal/mol. The pressure-dependent rate expression for $HNO_2(+M) \leftrightharpoons HONO(+M)$ at 700–1300 K: $k_{61,\infty} = 2.5 \times 10^{14} \exp(-49700/RT)$ 1/s and $k_{61,0} = 3.1 \times 10^{18} \exp(-48900/RT)$ cm^3/(mol s) with a fitted $F_{cent,61} = 1.149 \exp(-T/3125)$ was estimated from a QRRK analysis. However, calculations of Eckart barriers [116] for H-atom tunneling facilitated a substantial reduction of the activation energies by 17.4 kcal/mol leading to the final expression of k_{61} found in Table IV. Note that this corresponds to an acceleration of the reaction rate by about 3–4 orders of magnitude within the considered temperature range.

The recombination reaction between NO and O to form NO_2 (R31) is well-characterized across wide temperature and pressure intervals, i.e [117–120], and old [121] and recent [41] reviews are generally in good agreement. The present mechanism uses high- and low-pressure limits from Tsang and Herron including falloff parameters. The pressure-dependent rate constant in Table IV is valid for N_2 as collision partner, but a separate expression for M = Ar is also available from [121].

The reaction $NO_2+H \leftrightharpoons NO+OH$ (R34) is an important source of OH radicals. A large body of experimental data are available in the low-to-intermediate-temperature range [41], but comparison of the measurements reveals significant scatter; especially at temperatures above 400 K. We have adopted the rate constant proposed by Ko and Fontijn [122]. Ab initio calculations indicate that (R34) completely predominates over the stabilization of the unimolecular products, i.e. $NO_2+H(+M) \leftrightharpoons HNO_2/HONO(+M)$, except at high-pressure/low-temperature conditions (>100 bar and <298 K) beyond those relevant to this study.

The reaction between NO_2 and O has two competing product channels. Most experimental data on the bimolecular channel (R37) fall in the low-temperature

Table IV Reactions from the N/H/O Subset

	Reactions	A	β	E	Note/Reference
30.	NO + H(+M) $\rightleftharpoons$ HNO(+M^a)	1.52×10^{15}	−0.41	0	[121]
	Low pressure limit:	2.36×10^{14}	0.206	−1550	[171]
	Troe parameters: 0.82 10^{-30} 10^{30}				
31.^{b}	NO + O(+M) $\rightleftharpoons$ NO$_2$(+M)	1.30×10^{15}	−0.75	0	[121]
	Low pressure limit:	4.72×10^{24}	−2.87	1550	[121]
	Troe parameters: 0.88 10^{-30} 10^4				1 bar
	Troe parameters: 0.87 10^{-30} 10^{30}				10 bar
	Troe parameters: 0.85 10^{-30} 10^{30}				20 bar
	Troe parameters: 0.82 10^{-30} 10^{30}				50 bar
	Troe parameters: 0.78 10^{-30} 10^{30}				100 bar
32.	NO + OH(+M) $\rightleftharpoons$ HONO(+M)	1.10×10^{14}	−0.3	0	[128]
	Low pressure limit:	3.39×10^{23}	−2.5	0	[128]
	Troe parameters: 0.75 10^{-30} 10^{30}				
33.	NO + HO$_2$ $\rightleftharpoons$ NO$_2$ + OH	2.05×10^{12}	0.0	−500	[41]
34.	NO$_2$ + H $\rightleftharpoons$ NO + OH	1.32×10^{14}	0.0	362	[122]
35.^{c}	NO$_2$ + H$_2$ $\rightleftharpoons$ HONO + H	1.30×10^4	2.76	29770	[145]
36.^{c}	NO$_2$ + H$_2$ $\rightleftharpoons$ HNO$_2$ + H	8.43×10^3	2.635	32550	This study
37.^{c}	NO$_2$ + O $\rightleftharpoons$ NO + O$_2$	1.05×10^{14}	−0.52	0	[124]
38.^{c}	NO$_2$ + O(+M) $\rightleftharpoons$ NO$_3$(+M)	3.52×10^{12}	0.24	0	[126]
	Low pressure limit:	2.45×10^{20}	−1.5	0	[126]
	Troe parameters: 0.71 10^{-30} 1700				
39.	NO$_2$ + OH(+M) $\rightleftharpoons$ HONO$_2$(+M)	3.00×10^{13}	0.0	0	[136]
	Low pressure limit:	2.94×10^{25}	−3.0	0	[136]
	Troe parameters: 0.4 10^{-30} 10^{30}				
40.	NO$_2$ + HO$_2$ $\rightleftharpoons$ HONO + O$_2$	1.91×10^0	3.32	3044	This study
41.	NO$_2$ + HO$_2$ $\rightleftharpoons$ HNO$_2$ + O$_2$	1.85×10^1	3.26	4983	This study
42.	NO$_2$ + NO$_2$ $\rightleftharpoons$ NO + NO + O$_2$	4.51×10^{12}	0.0	27600	[145]
43.	NO$_2$ + NO$_2$ $\rightleftharpoons$ NO$_3$ + NO	9.64×10^9	0.73	20900	[121]
44.	NO$_2$ + NO(+M) $\rightleftharpoons$ N$_2$O$_3$(+M)	1.62×10^9	1.4	0	[123]
	Low pressure limit:	1.33×10^{33}	−7.7	0	[123]
	Troe parameters: 0.6 10^{-30} 10^{30}				
45.	NO$_2$ + NO$_2$(+M) $\rightleftharpoons$ N$_2$O$_4$(+M)	6.00×10^{12}	0.0	0	[123]
	Low pressure limit:	1.31×10^{24}	−3.8	0	[123]
	Troe parameters: 0.4 10^{-30} 10^{30}				
46.	NO$_2$ + CO $\rightleftharpoons$ NO + CO$_2$	9.00×10^{13}	0.0	33800	[149]
47.	NO$_3$ + H $\rightleftharpoons$ NO$_2$ + OH	6.00×10^{13}	0.0	0	[172]
48.	NO$_3$ + O $\rightleftharpoons$ NO$_2$ + O$_2$	1.00×10^{13}	0.0	0	[68]
49.	NO$_3$ + OH $\rightleftharpoons$ NO$_2$ + HO$_2$	1.40×10^{13}	0.0	0	[68]
50.	NO$_3$ + HO$_2$ $\rightleftharpoons$ NO$_2$ + O$_2$ + OH	1.50×10^{12}	0.0	0	[172]
51.	NO$_3$ + NO$_2$ $\rightleftharpoons$ NO$_2$ + NO + O$_2$	5.00×10^{10}	0.0	2940	[173]
52.	HNO + H $\rightleftharpoons$ NO + H$_2$	4.40×10^{11}	0.72	650	[174]
53.	HNO + O $\rightleftharpoons$ NO + OH	2.30×10^{13}	0.0	0	[157]
54.	HNO + OH $\rightleftharpoons$ NO + H$_2$O	1.30×10^7	1.88	−956	[175]
55.	HNO + O$_2$ $\rightleftharpoons$ HO$_2$ + NO	2.20×10^{10}	0.0	9140	[176]
56.^{c}	HNO + NO$_2$ $\rightleftharpoons$ HONO + NO	4.42×10^4	2.64	4040	[156]
57.	HONO + O $\rightleftharpoons$ NO$_2$ + OH	1.20×10^{13}	0.0	5960	[121]
58.	HONO + OH $\rightleftharpoons$ NO$_2$ + H$_2$O	1.70×10^{12}	0.0	−520	[155]
59.	HONO + NO$_2$ $\rightleftharpoons$ HONO$_2$ + NO	2.00×10^{11}	0.0	32700	[145]
60.	HONO + HONO $\rightleftharpoons$ NO + NO$_2$ + H$_2$O	3.49×10^{-1}	3.64	12140	[177]

Continued

Table IV Continued

	Reactions	A	β	E	Note/Reference
61.	$HNO_2(+M) \rightleftharpoons HONO(+M)$	2.50×10^{14}	0.0	32300	This study
	Low pressure limit:	3.10×10^{18}	0.0	31500	This study
	Troe parameters: 1.149 10^{-30} 3125				
62.	$HNO_2 + O \rightleftharpoons NO_2 + OH$	1.70×10^{8}	-1.5	2000	[108]
63.	$HNO_2 + OH \rightleftharpoons NO_2 + H_2O$	4.00×10^{13}	0.0	0	This study
64.	$HONO_2 + H \rightleftharpoons H_2 + NO_3$	5.56×10^{8}	1.5	16400	[178]
65.	$HONO_2 + H \rightleftharpoons H_2O + NO_2$	6.08×10^{1}	3.3	6285	[178]
66.	$HONO_2 + H \rightleftharpoons OH + HONO$	3.82×10^{5}	2.3	6976	[178]
67.	$HONO_2 + OH \rightleftharpoons H_2O + NO_3$	1.03×10^{10}	0.0	-1240	[179]

Units are mol, cm, s, cal.

[a] Enhanced third-body efficiency: $N_2 = 1.6$.

[b] Troe parameters fitted to center broadening factor $F_c = 0.95 - 1 \times 10^{-4}T$ [121].

[c] Reverse Arrhenius parameters available in the reference.

region [121,123]. Bemand et al. [124] measured k_{37} at temperatures from 298–1055 K with an overall uncertainty factor of 1.37 using two independent discharge flow systems. Tsang and Herron [121] recommended the slightly higher low-temperature estimate (230–350 K) by Atkinson et al. [125], but extended the temperature range to 200–2500 K, while keeping the original uncertainty factor of 1.2 from [125]. At temperatures below 350 K, the discrepancy between [124] and [121] is less than 10%, but it increases at higher temperatures to yield values outside the uncertainty limit above 1200 K. In this study, the rate constant from Bemand et al. is preferred due to the extented temperature validation. Experimental characterization of the competing addition reaction to NO_3 (R38) is restricted to the low-temperature region. Tsang and Herron [121] recommended the high-pressure limit from Atkinson et al. [125] (200–400 K) with an uncertainty factor of 2 together with an extrapolated low-pressure limit to account for an extended temperature range of 200–2500 K and N_2 as collision partner. The rate constant used in the present mechanism is taken from Hahn et al. [126], who performed an experimental and theoretical study of the temperature and pressure dependence of (R38). Hahn et al. used laser flash-photolysis experiments combined with trajectory calculations on standardized valence potentials of the involved species at conditions ranging from 300–400 K and 1–900 bar N_2 atmosphere. The proposed rate constant agrees well with values from Tsang and Herron at temperatures and pressures below 500 K and 100 bar. Further extrapolation to e.g., 800 and 1100 K, however, yields values that are about a factor of 1.5–2 larger than Tsang and Herron.

The addition reactions of OH with NO and NO_2 to form HONO (R32) and $HONO_2$ (R39) play important roles in the HO_x cycle by either consuming or liberating (through reverse reactions) OH radicals depending on the reaction conditions. In the present study, (–R32) is expected to gain particular importance as a major OH formation channel due to the establishment of a significant HONO pool from $NO_2+H_2 \rightleftharpoons HONO+H$ (R35), $NO_2+HO_2 \rightleftharpoons HONO+O_2$ (R40), and isomerization of HNO_2 (R61). The addition reaction $NO+OH(+M) \rightleftharpoons HONO(+M)$ has only been studied at lower temperatures in the range of 100–500 K [121,123]. Tsang and Herron [121] based their recommendation on available low-temperature data combined with transition state and RRKM calculations to extend the temperature and pressure range and yield high- and low-pressure limits at temperatures up to 2500 K with N_2 as bath gas. They accompanied their final rate expression with an uncertainty factor ranging from 1.4 at room temperature to a value of 3 at the highest temperature. Recent experimental investigations of the pressure dependence of (R32) by Forster et al. [127] (1–150 bar) and Fulle et al. [128] (1–1400 bar) both apply He as bath gas and maximum temperatures of 298 and 400 K, respectively. The pressure-dependent rate constant proposed by Fulle et al. matches the recommendation by Tsang and Herron at low pressures and/or high temperatures, but exceeds it by more than a factor of 4 at 100 bar and temperatures relevant to this study. Despite the uncertainties related to the temperature extrapolation and change of collision partner, the present mechanism includes the rate constant from Fulle et al.

Experimental data on the NO_2+OH addition reaction (R39) are available at low temperatures (<480 K) [123, 129–131], while a few dissociation experiments are reported at 800–1200 K, e.g. [132,133]. At high pressures, the reaction is complicated by competitive formation of the HOONO isomer [131,134–135]. Troe

[136] conducted a theoretical analysis of the temperature and pressure dependence of (R39) over the range 50–1400 K and pressures up to 1000 bar. Troe also considered the impact from possible formation of HOONO based on an estimated rate expression, and found it to be negligible at pressures below 1 bar, whereas yields up to 20% are likely at 100 bar and 200–400 K. HOONO is also the intermediate adduct in the important OH formation reaction NO+HO$_2$ ⇌ NO$_2$+OH (R33), which is favored by a large HO$_2$ radical pool and, therefore, most likely runs in the forward direction at conditions relevant to this study. Consequently, it is expected that the net-flux through HOONO favors redissociation back to NO$_2$+OH. The rate constant is adopted from the work of Troe [136]. It is consistent with the available experimental data to a satisfying degree even though the accuracy of estimated values of F_{cent}, $k_{39,0}$ and $k_{39,\infty}$ in [136] is limited by uncertainties in a number of unknown molecular parameters.

A recent flow reactor and detailed kinetic modeling study of NO$_x$/hydrocarbon interactions by Glarborg et al. [137] identified NO$_2$+HO$_2$ ⇌ HONO+O$_2$ (R40) as an important HO$_2$ removal channel in competition with HO$_2$+HO$_2$ ⇌ H$_2$O$_2$+O$_2$ (R15) and NO+HO$_2$ ⇌ NO$_2$+OH (R33). Glarborg et al. used k_{40} = $6.3 \times 10^7 T^{1.25} \exp(-5000/RT)$cm^3/mol s from Hori et al. [138], whose estimate complies with the room temperature upper limit [139] and rate constant data derived from high-temperature shock tube measurements by Glänzer and Troe [140]. The accuracy of the latter results are, however, in question due to uncertainties in important side reactions. Chan and Pritchard [141] recently published an ab initio study of important reactions from the HNO$_2$ subset including recommendations for both k_{40} and k_{41}. These calculations favored the HNO$_2$−O$_2$ product channel (R41) over HONO+O$_2$ (R40) by more than a factor of 2 at temperatures above 500 K, and suggested that the overall rate constant for NO$_2$+HO$_2$ should be one to five orders of magnitude lower than the estimate by Hori et al. at temperatures ranging from ∼2000 K toward ambient. Ab initio CBS-QB3 calculations carried out as part of the present work (Fig. 7) indicate that at subambient temperatures, NO$_2$ and HO$_2$ predominantly add to form stabilized HOONO$_2$, as described by Gierczak et al. [142]. However, this pathway is suppressed at elevated temperatures, including those considered in the present work. Here, the reactants instead form a hydrogen bonded adduct at the entrance of the reaction coordinate favoring the orientation leading to HONO+O$_2$ (H···N association is weaker than H···O for NO$_2$). While hydrogen bonding stabilizes the transition state to HONO+O$_2$, it also makes the entropy unfavorable, and consequently, the reaction to
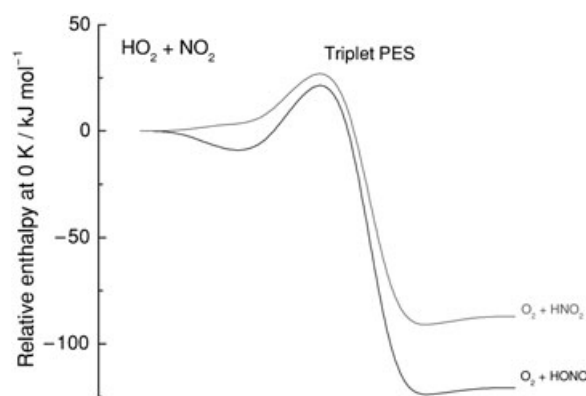
Figure 7 Potential energy diagram for NO$_2$ + HO$_2$ based on CBS-QB3 calculations, showing relative enthalpies at 0 K.

HONO+O$_2$ is slower relative to HNO$_2$+O$_2$ at increasing temperatures. The predicted rate expressions for k_{40} and k_{41} (Table IV) imply that $k_{41}/k_{40} > 1$ at temperatures roughly >500 K, and the ratio yields values of 2.4 and 3.3 at 1000 and 1500 K, respectively. The overall rate constant $k_{40} + k_{41}$ is more than 10 times lower than the expression from Hori et al. [138], but substantially higher than the calculated rate constants from Chan and Pritchard [141].

The reactions NO$_2$+H$_2$ to HONO+H (R35) and HNO$_2$+H (R36) constitute the principal initiation reactions in the H$_2$/NO$_x$ system. Tsang and Herron [121] recommended the use of k_{35} originally proposed by Slack and Grillo [143] based on shock tube measurements of the ignition delay of H$_2$/air mixtures pertubated with NO$_2$ at 760–1000 K and 1–4 bar. Tsang and Herron assigned a high uncertainty factor of 5 to this rate expression. More recent investigations [2,144–145] indicate that k_{35} should be somewhat lower. Expressions of k_{35} and k_{-35} were derived by Park et al. [145] based on ab initio calculations with transition state parameters from Hsu et al. [146]. These rate constants are in good agreement with the single flow reactor measurement at 833 K reported by Mueller et al. [144]. No previous reports have mentioned the alternative product channel to HNO$_2$+H (R36).

Ab initio CBS-QB3 calculations indicate that (R36) is unimportant at temperatures roughly <1600 K, while it constitutes ∼10% of the product yield from NO$_2$+H$_2$ at temperatures >1600 K. The calculations yield the expression $k_{36} = 2.43T^{3.73} \exp(-16306/T)$ cm^3/(mol s) across the temperature range 700–2000 K. They include an Eckart tunneling correction [116], which contributes less than a factor of 1.45 within the investigated temperature range. Similarly, the predicted expression of $k_{35} = 12.4T^{3.70} \exp(-14733/T)$ cm^3/(mol s) with a tunneling correction yielding less

than a factor of 1.2. The latter is in close agreement with the previous value of k_{35} from Park et al. [145]. The experimental studies of NO_2+H_2 by Slagle and Grillo [143] and Mueller et al. [144] were both conducted at temperatures <1000 K, where formation of HNO_2 is negligible, so it is unlikely that previous rate determinations of k_{35} have been subjected to interference from (R36). The present mechanism includes the calculated expressions of k_{35} and k_{36} from Park et al. [145] and from the present calculations, respectively, even though it is evident that (R35) will be the dominant product channel at conditions relevant to the present work.

Reactions are available to account for the conversion between NO, NO_2 (R42), NO_3 (R43, R51), and the dimers N_2O_3 (R44) and N_2O_4 (R45). The conversion is driven by increasing pressure and availability of molecular oxygen, e.g. through $NO+NO+O_2 \rightleftharpoons NO_2+NO_2 \rightleftharpoons N_2O_4$, whereas increasing temperatures promote the reverse decomposition reactions. A shock tube study of the thermal decay of NO_2 by Röhrig et al. [119] has recently provided experimental data for (R42) and (R43) at high temperatures (1350–2100 K). Park et al. [145] combined these data for (R42) with pyrolysis measurements for NO_x at intermediate temperatures (602–954 K) to obtain an expression of k_{42} across the temperature range 600–1450 K. Data of (–R42) are also available at intermediate temperatures: Olbregts [147] conducted static reactor experiments with NO/O_2 mixtures at temperatures from 226 to 758 K to yield an expression of k_{-42} that agrees within 15% of the expression of Park et al. at temperatures from 600 to 1450 K, when using thermodynamic data from Table I to calculate k_{42}. The rate of the bimolecular channel $NO_2+NO_2 \rightleftharpoons NO_3+NO$ (R43) from Tsang and Herron [121] is in excellent agreement with the recent high-temperature measurements by Röhrig et al. [119] at 1350–2100 K.

The direct oxidation of CO by NO_2 (R46) has been characterized in a number of experimental studies. The high-temperature shock tube measurements by Milks et al. [148] and Freund and Palmer [149,150] from the late 70s are all in excellent agreement. These evaluations are also consistent with earlier studies at moderate to high temperatures (500–1500 K), e.g. [151–154]. Against this background, Tsang and Herron [121] recommended the use of the rate constant from [149] including the original experimental uncertainty factor of 2.5. The present mechanism follows this recommendation.

Subsets for HNO, $HONO/HNO_2$, $HONO_2$, and NO_3 are drawn from literature mechanisms [2,107–108,111,145] with updates from recent elementary reaction studies [155–158] and the present calculations. Most important are the termination reactions $HONO/HNO_2+OH \rightleftharpoons NO_2+H_2O$ (R58, R63); and the HONO formation channels $HNO+NO_2 \rightleftharpoons HONO+NO$ (R56) and $HNO_2(+M) \rightleftharpoons HONO(+M)$ (R61) that indirectly produce OH radicals through subsequent decomposition of HONO.

EXPERIMENTS AND NUMERICAL APPROACH

Mixtures of CO, H_2, O_2, and NO_x highly diluted in N_2 have reacted at three different pressures: 100, 50, and 20 bar under oxidizing conditions ($\phi = 0.06$). The addition of NO_x had a dual purpose. First of all, the reaction kinetics of NO_x is an important subset in many combustion systems, and experiments with only $CO/H_2/O_2$ provided an opportunity to test the proposed NO_x mechanism at conditions that did not involve direct NO_x/hydrocarbon interactions. The second purpose rose from the fact that the experimental system is limited to operations <925 K. However, NO_x has a promoting effect on the fuel initiation that enabled measurements of reactant conversion at lower temperatures than otherwise obtained with pure CO/H_2 oxidation.

The experimental conditions are summarized in Table V. τ denotes the temperature-dependent residence time in the isothermal section of the reactor calculated from Eq. (1). The diluted conditions ensured a low heat development during the reaction, and calculations of the adiabatic temperature rise indicate values <8 K for all conducted experiments. The carbon balance closed within 1% in all three experiments. The experimental data are obtained as mole fractions as a function of the reactor temperature in the isothermal section from 600 to 900 K using intervals of 25 K. The lower bound of the temperature interval (600 K) is well below the temperature where the CO/H_2 conversion initiates. The results are shown in Fig. 8 with the 100 bar experiment at the top. Figure 8 also includes numerical predictions of the concentration profiles obtained from plug flow simulations using the Senkin code [159] from the Chemkin–II library [160]. Here, $t = 0$ and $t = \tau$ corresponds to the inlet and outlet of the isothermal reaction zone, respectively.

NO_x was supplied to the system as pure NO diluted in N_2. However, the high pressure and excess O_2 promoted a substantial conversion of NO to NO_2 prior to the reactor inlet via $NO + NO + O_2 \rightleftharpoons NO_2 + NO_2$ (–R42). This was detected by measurements conducted at reactor temperatures below the fuel initiation temperature (<600 K) and was verified by simulations. The resulting inlet distribution of NO_x species is reflected in the reactant concentrations listed in Table V. It is expected that a similar conversion of NO_x

Table V   Reaction Conditions Applied during Experiments with CO/H$_2$/NO$_x$. The Reactant Concentrations Are Balanced by N$_2$. The Volumetric Flow Rate Was ~3 NL/min in all Experiments.

	Reactant Concentrations							
Exp. id.	CO (ppm)	H$_2$ (ppm)	O$_2$ (%)	NO$_x$(NO) (ppm)	Pres. (bar)	Temperature (K)	ϕ^a	τ (s K)
A	502	440	1.48	151(6)	100	598–898	0.064	11990/T
B	518	446	1.54	151(26)	50	598–898	0.063	6030/T
C	518	453	1.53	149(113)	20	598–898	0.063	2350/T

^{a} Stoichiometric ratio (ϕ) is based on CO + H$_2$ + O$_2$ → CO$_2$ + H$_2$O.
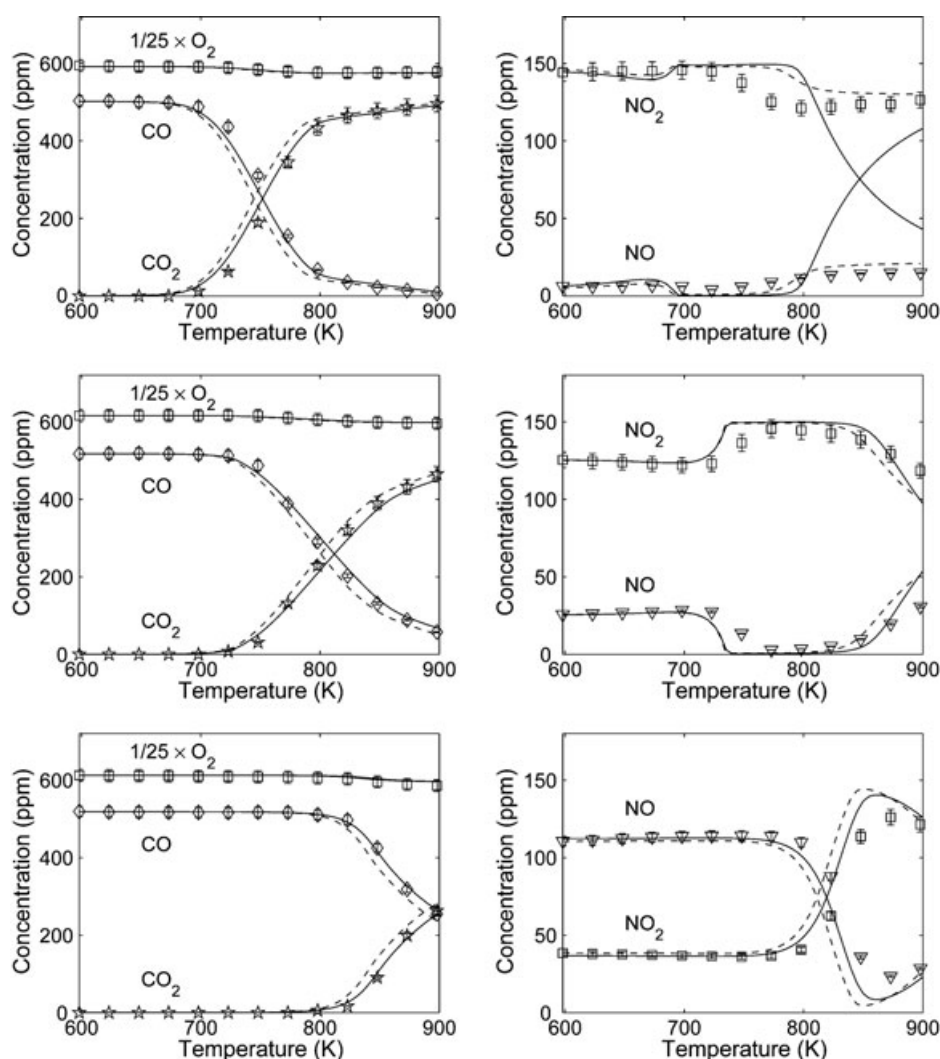
Figure 8   Experimental and modeling results of CO/H$_2$/NO$_x$ experiments. Concentration profiles are shown as a function of the reactor temperature at 100 (top), 50 (middle) and 20 bar (bottom) cf. experiments A–C. Reaction conditions are provided in Table V. Symbols mark experimental results, whereas full lines denote model predictions obtained at isothermal conditions using the temperature-dependent residence times from Table V. Dashed lines represent simulations with the experimental temperature profiles; see text. Measuring uncertainties are ±2.6% for O$_2$/CO, ±4.3% or ±3 ppm for CO$_2$, and ±2.8 and 4.0% for NO and NO$_2$, respectively.

may take place after the product gas has left the isothermal reaction zone, but before the pressure is reduced to atmospheric level and product analysis is completed. To clarify this issue, NO and NO_2 profiles are calculated both under the assumption that conversion takes place solely in the isothermal section of the reactor tube and throughout the entire reactor tube represented by the full experimental temperature profiles.

DISCUSSION

The numerical predictions of the measured concentration profiles in Fig. 8 are satisfactory for all the experiments. It is noteworthy that the concentration profiles from all three experiments display similar trends, even though they appear at different temperatures. This suggests a similar governing chemistry in all the experiments. The results reveal a decreasing CO initiation temperature from about 800 to 700 K when the pressure increases from 20 to 100 bar. The most significant decrease takes place between 20 and 50 bar, which suggests a declining pressure dependency with increasing pressure. Simulations with varying residence times have confirmed that this behavior is a result of increasing pressure, rather than an effect of increasing residence times.

Deviations between modeling results obtained at isothermal conditions (full lines in Fig. 8) and with the complete experimental temperature profiles (dashed lines) are minor except at the highest pressure and temperatures >800 K, where the behavior of the NO_x profiles is only accurately captured by the model when applying the full temperature profiles. This is in line with the previous discussion of the potential conversion of NO_x outside the isothermal section of the reactor.

The results of a reaction path analysis and a first-order sensitivity analysis based on the kinetic model are shown in Figs. 9–11. The fuels CO and H_2 are oxidized to the stable products CO_2 and H_2O by reaction with OH radicals; either directly (R24) or, in the case of CO, through intermediate formation of HOCO (R25) and subsequent oxidation by molecular oxygen via (R29). Hydroxyl is then generated through reactions of HO_2 and H in a number of steps that involve recycling of NO/NO_2.

There is no significant contribution from reactions between CO and other potential reactants, e.g. HO_2 and O_2. However, at 100 bar, a number of CO consumption reactions show up in the sensitivity analysis even though they contribute little in terms of flux; these include CO+HO_2 and CO+NO_2, as well as formation of HCO through H+CO recombination (Fig. 11). The model indicates that (R29) completely dominates over
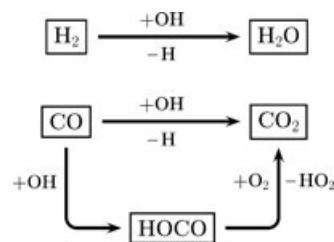
Figure 9 Major reaction pathways for CO/H_2 conversion at the investigated conditions of experiment A–C.
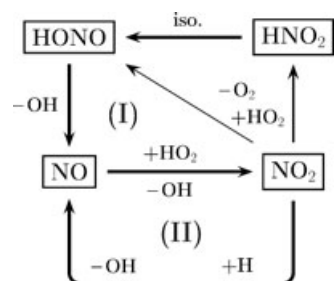

Figure 10 NO_x interactions with the H/O radical pool are the main source of OH radicals at the investigated conditions of experiment A–C. The sums of the two sequences yield (I): $HO_2 + HO_2 \rightleftharpoons OH + OH + O_2$, (II): $HO_2 + H \rightleftharpoons OH + OH$.

the unimolecular decomposition of HOCO (R26) independently of ϕ and pressure. The ratio 29/(24 + 29) increases with increasing pressure and/or low temperatures. Hence, at 750 K, about 75% and 60% of the CO conversion during the 100 and 50 bar experiments involve intermediate HOCO formation. At 900 K, these contributions have decreased to about 50% and 35% respectively. In the 20 bar experiment, the importance of (R29) is reduced to <30%.
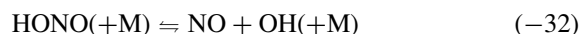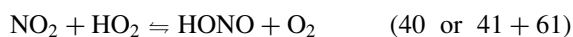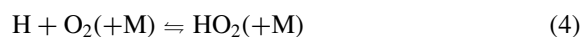
The two NO/NO_2 recycling sequences (I) and (II) in Fig. 10 are the major sources of the important chain-carrying OH radicals at the investigated conditions. Hydroperoxyl is the sole radical reactant in (I). First, NO is oxidized to NO_2 followed by reduction to HONO; either directly via (R40), or through intermediate formation and isomerization of HNO_2 (R41)+(R61). Nitrous acid readily decomposes to NO+OH (–R32) and completes the cycle, while yielding a net formation of two OH radicals. About 2/3 of the nitrogen flux in (I) passes through HNO_2, but the HNO_2 pool remains very low due to rapid isomerization to HONO. In mechanism (II), NO is directly regenerated from NO_2 through reaction with H atoms (R34). This also yields a net formation of two OH radicals per cycle at the expense of HO_2+H.

The ratio between the two NO/NO_2 cycles is controlled by the availability of H and HO_2 radicals. Hydrogen atoms are produced from the direct conversion of H_2 to H_2O (R9), and CO to CO_2 (R24), but
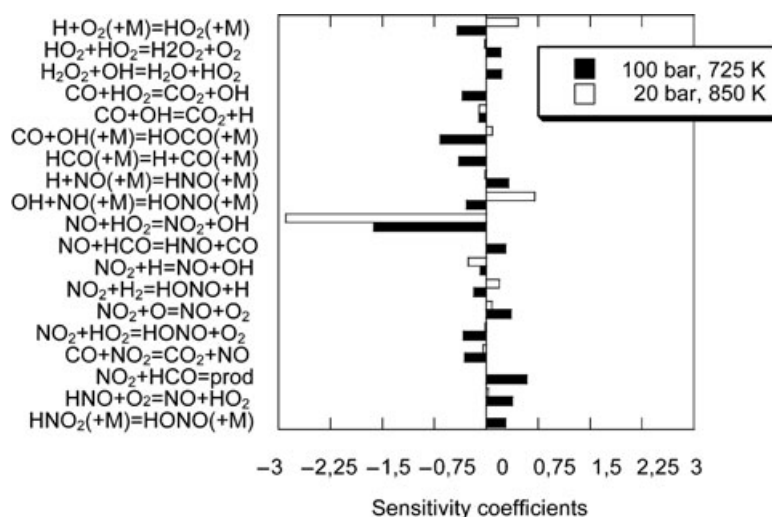
Figure 11 First-order sensitivity analysis for CO at 100 bar (725 K) and 20 bar (850 K), respectively.

at high pressure and/or low temperatures a considerable fraction of the H atom pool is converted to HO$_2$ through H+O$_2$(+M) $\leftrightharpoons$ HO$_2$(+M) (R4), thereby promoting (I) over (II). The calculations indicate that the ratio (I)/(II) $\approx$ 4/34 that yields values >5 at 100 bar and 750 K. The ratio decreases with the temperature to $\sim$3.5 at 900 K. At 50 bar, the ratio is below unity, and at 20 bar or below, reaction (R34), i.e. sequence (II), dominates completely. It is noticed that the introduction of (R4) as a source of HO$_2$ radicals in mechanism (I) makes the net gain from the two pathways identical, as illustrated below:

$$H + O_2(+M) \leftrightharpoons HO_2(+M) \tag{4}$$

$$NO_2 + HO_2 \leftrightharpoons HONO + O_2 \qquad (40 \text{ or } 41 + 61)$$

$$HONO(+M) \leftrightharpoons NO + OH(+M) \tag{-32}$$

$$\Sigma \quad NO_2 + H \leftrightharpoons NO + OH \tag{34}$$

This means that the general reactivity of the system is conserved at all investigated pressures even though the underlying mechanism changes. This is consistent with the almost identical shapes of the CO conversion profiles observed in Fig. 8.
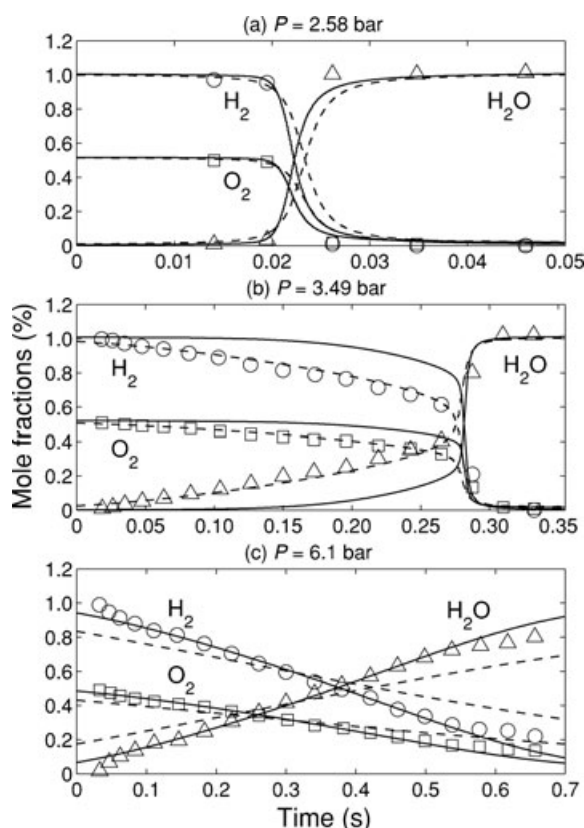
COMPARISON WITH LITERATURE DATA

The new experimental data presented on the lean CO/H$_2$/O$_2$/NO$_x$ system offer verification of only a limited subset of the kinetic model. To extend the model validation, this section presents additional comparisons between modeling results and experimental data on the

H$_2$/O$_2$, H$_2$/O$_2$/NO$_2$, CO/H$_2$O/O$_2$, and CO/H$_2$/O$_2$ systems at medium temperatures and ambient to elevated pressures obtained from the literature.

Flow Reactor Results

We first consider a series of flow reactor experiments [1,2,161] conducted in the Princeton flow reactor at pressures from 1 to 10 bar and medium temperatures. These results are shifted in time to match the steepest gradient of the fuel conversion, which means that the beginning of the reaction zone ($t = 0$) is undefined and hence, also the onset of the simulations.
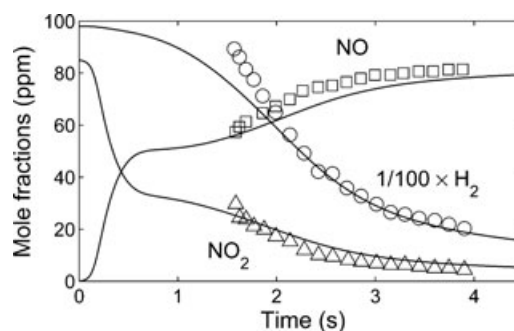
Results from the H$_2$/O$_2$ system diluted in N$_2$ [1] are shown in Figs. 12 at three different pressures. The model predictions marked by full lines are in good agreement with the measurements in Figs. 12a and 12c, but the initiation is faster in Fig. 12b than indicated here by the measurements. A pathway analysis based on the present model indicates that the H$_2$/O$_2$ system at moderate temperatures and elevated pressure conditions is controlled by a cyclic conversion of H/O radical species; illustrated in Fig. 13, where the conversion of the comparatively slow-reacting species HO$_2$ and H$_2$O$_2$ is limiting. As shown in Fig. 13, the major sinks for H$_2$ are the reactions with OH (R9) and HO$_2$ (–R17). These reactions compete with the termination step HO$_2$+OH $\leftrightharpoons$ H$_2$O+O$_2$ (R14). As previously discussed, reaction (R14) exhibits a marked minimum in the rate constant at temperatures around 1000 K (Fig. 5). Mueller et al. [1] proposed a detailed kinetic model that accurately predicted the results of all three experiments in Fig. 12. However, they used a value for k_{14} [162] that complies with the non-Arrhenius

Figure 14 Comparison between experimental data from Mueller et al. [2] and model predictions for the $H_2/O_2/NO_2/N_2$ system at 10 bar. Inlet conditions are 0.98% H_2, 0.50% O_2, 85 ppm NO_2, bal. N_2, and $T_{in} = 780$ K. Simulations (lines) are conducted as adiabatic plug flow calculations using the present kinetic model and include timeshifts to match the steepest gradient of the fuel conversion.

Figure 12 Comparison between experimental data from Mueller et al. [1] and model predictions for the $H_2/O_2/N_2$ system at stoichiometric conditions and three different pressures. Inlet concentrations are everywhere: 1.01% H_2, 0.52% O_2, and bal. N_2. Furthermore: (a) $P = 2.58$ bar, $T_{in} = 935$ K; (b) $P = 3.49$ bar, $T_{in} = 933$ K; (c) $P = 6.1$ bar, $T_{in} = 934$ K. Simulations (lines) are conducted as adiabatic plug flow calculations and include timeshifts to match the steepest gradient of the fuel conversion. Full lines denote simulations with the present kinetic model from Tables I–IV. Dashed lines represent simulations using the rate constant of $HO_2 + OH \rightleftharpoons H_2O + O_2$ (R14), $k_{14} = 2.89 \times 10^{13} \exp(500/[RT])$ cm^3/(mol s), from Baulch et al. [162] (advocated by Mueller et al. [1]) instead of k_{14} proposed in the present work, cf. Fig. 5.
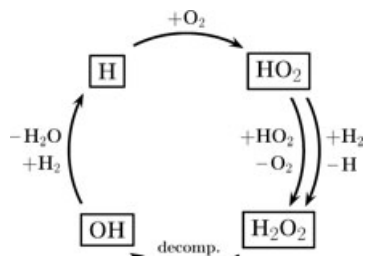
Figure 13 Major reaction pathways for H_2/O_2 conversion at medium temperatures and elevated pressure conditions.

behavior of the reaction only at temperatures roughly below 700 K. At 933 K, their value is larger than $k_{14,\text{present work}}$ by a factor of 3.5. This has a substantial impact on the model predictions, as observed in Fig. 12, where dashed lines denote simulations with $k_{14,\text{Baulch et al., 1994}}$ instead of $k_{14,\text{present work}}$. Note that the forced timeshift is larger with $k_{14,\text{Baulch et al., 1994}}$ (dashed lines) consistent with a slower initiation. Interestingly, this single modification of the present model results in a good prediction of the experimental results in Fig. 12b, whereas poor agreement is obtained in Fig. 12c. There is substantial experimental evidence of $k_{14,\text{present work}}$ in the considered temperature range (Fig. 5) to accept this rate constant as more reliable, but this suggests that the overall kinetic scheme may still be incomplete. At present, this issue remains unresolved.

Figure 14 shows good agreement between model predictions and measurements [2] on the $H_2/O_2/NO_2/N_2$ system at 10 bar and $T_{in} = 780$ K. Pathway analysis indicates that the H/O radical pool is dominated by reactions with NO_x in general agreement with the mechanism in Fig. 10, and hence, provides an additional confirmation of this part of the model.

Figure 15 shows a comparison between model predictions and experiments [161] from the $CO/H_2O/O_2/N_2$ system at ambient pressure and slightly higher temperatures from 1033–1100 K. The governing chemistry is shown in Fig. 16 derived from pathway analysis based on the kinetic model. Compared to the reaction network for pure H_2/O_2 conversion at elevated pressures in Fig. 13, the main differences are the increasing importance of $H+O_2 \rightleftharpoons O+OH$ (R3) and $HO_2+H \rightleftharpoons OH+OH$ (R11) that both lead to OH radicals and thereby promote reaction. Hydrogen atoms are almost exclusively formed from
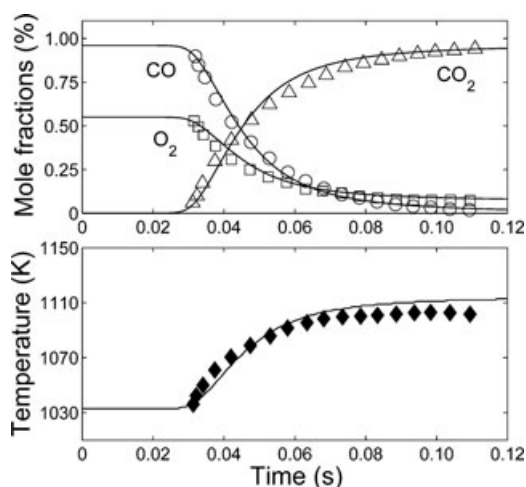
Figure 15 Comparison between experimental data from Yetter et al. [161] and model predictions for the CO/H$_2$O/O$_2$/N$_2$ system at 1 bar. Inlet conditions are: 0.96% CO, 0.56% H$_2$O, 0.55% O$_2$, bal. N$_2$, and $T_{in} = 1033$ K. Simulations (lines) are conducted as adiabatic plug flow calculations using the present kinetic model and include timeshifts to match the steepest gradient of the fuel conversion.
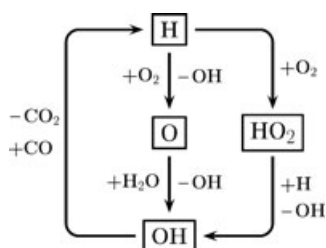

**Figure 16** Major reaction pathways for CO/H$_2$O/O$_2$ conversion at ∼1000–1100 K and ambient pressure.

CO+OH $\rightleftharpoons$ CO$_2$+H (R24) in the absence of H$_2$ in the fuel. The good agreement between experimental and modeling results indicates that the model is well representative of this chemistry.

Syngas Ignition Delay

There has been a recent interest in the synthesis gas ignition times at elevated pressures and lower temperatures [9,11,21,98] with practical applications for engines and gas turbines. Syngas is an important alternative fuel as well as a chemical feedstock. It is derived from fossil fuels and consists mainly of H$_2$ and CO with varying concentrations of CO$_2$ and other gases. The kinetics of CO/H$_2$ conversion is generally considered to be well-known. Nevertheless, Petersen et al. [21] have recently demonstrated that there is a substantial discrepancy between the predictions of state-of-art detailed kinetic models [19,99,163–165] and experi-
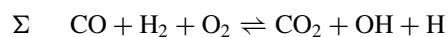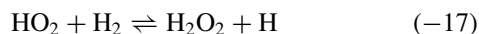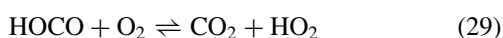
mental data obtained in flow reactors [12,166], shock tube [21], and a rapid compression machine [11] for a common syngas mixture of 7.33% H$_2$, 9.71% CO, 1.98% CO$_2$, 17.01% O$_2$, 63.97% N$_2$ at 20 bar and temperatures from 600 to 950 K. In this temperature range, the models consistently predict ignition times that are up to five orders of magnitude above experiments. The reader is referred to the paper of Petersen et al. [21] for an elaborate discussion of the subject and further details about the referred experiments and previous modeling results.

Dryer and Chaos [167] recently rendered probable that the observed discrepancy could be explained by nonhomogeneous effects, such as catalyzed aberrations. However, in the present work we have looked at possible kinetic causes. Figure 17 shows a comparison between experiments and model predictions, similar to that in the paper of Petersen et al. [21], with the addition of the predictions made by our own model (full line). Calculations are conducted as adiabatic plug flow simulations at constant-volume conditions with the ignition delay time defined as the onset of a strong pressure rise corresponding to 50% increase of P within a very short time interval. Even though the present model predicts larger ignition times at low temperatures compared to the experiments, the figure shows a marked improvement over previous model performances. At the low-temperature conditions, the availability of
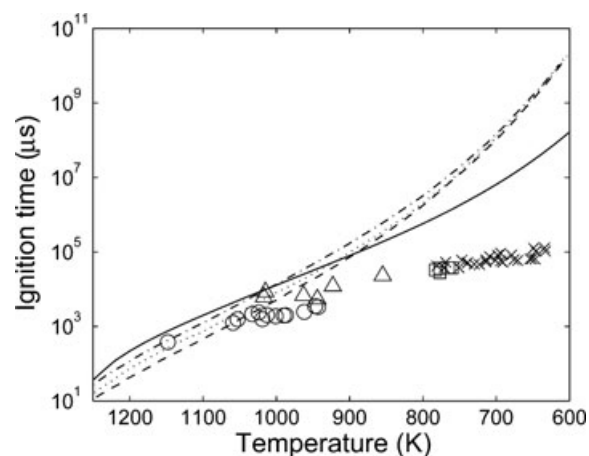
Figure 17 Comparison of ignition delay time data for syngas combustion. Symbols denote experimental results: × Peschke and Spadaccini [166] (flow reactor); □ and ○ Petersen et al. [21] (flow reactor and shock tube, respectively); △ Walton et al. [11] (RCM). Lines are model predictions using the mechanisms of: -·- Sun et al. [99]; ···Li et al. [164]; - - Saxena and Williams [165]; — This work. All calculations were conducted for the mixture: 7.33% H$_2$, 9.71% CO, 1.98% CO$_2$, 17.01% O$_2$, 63.97% N$_2$ at 20 bar. The figure is largely adopted from Petersen et al. [21].

reactive OH and H radicals is limited by the conversion of HO_2 and H_2O_2 in the presence of relatively high concentrations of CO, H_2, and O_2. A sensitivity analysis identifies $HO_2+H_2 \rightleftharpoons H_2O_2+H$ (−R17) and $CO+H_2O_2 \rightleftharpoons HOCO+OH$ (−R28) as the major bottlenecks. Petersen et al. [21] emphasized the importance of reaction $CO+HO_2 \rightleftharpoons CO_2+OH$ (R23), but the current modeling predictions are only sensitive to this reaction at temperatures >900 K. As previously discussed, the major consumption channel of HOCO is the reaction with molecular oxygen (R29), which gives rise to the overall mechanism

$$CO + H_2O_2 \rightleftharpoons HOCO + OH \qquad (-28)$$

$$HOCO + O_2 \rightleftharpoons CO_2 + HO_2 \qquad (29)$$

$$HO_2 + H_2 \rightleftharpoons H_2O_2 + H \qquad (-17)$$

$$\Sigma \quad CO + H_2 + O_2 \rightleftharpoons CO_2 + OH + H$$

that explains the sensitivity of these reactions.

The rate constants of (R17) and (R28) involve considerable uncertainties. The former is taken from Baulch et al. [41] and is based on limited experimental data with an assigned uncertainty factor of 3 at 300–1000 K, while the latter is estimated in the present work without experimental support and with an estimated uncertainty factor of 5. It is noted that maximum perturbations of k_{17} and k_{28} corresponding to these uncertainty limits yield a further reduction of the predicted ignition times of another decade at temperatures below 1000 K.

Although the current model provides a substantial improvement of the predicted syngas ignition times, Fig. 17 clearly shows that the discrepancy between experiments and kinetic models remains unresolved. It is conceivable that more accurate characterization of key reactions may lead to further improvements. However, nonhomogeneous effects, as proposed by Dryer and Chaos [167], are likely to be part of the explanation. Either way, additional experimental confirmation in the low-temperature region would be desirable, preferably in a system with negligible secondary effects.

CONCLUSIONS

This paper has presented a detailed description of a new laminar flow reactor made of quartz that is designed to conduct well-defined experimental investigations of homogeneous gas phase chemistry at high pressures up to 100 bar and moderate temperatures <925 K. The first results presented from this setup concern lean $CO/H_2/O_2/NO_x$ oxidation experiments at 20–100 bar and 600–900 K. These results have successfully been modeled using an updated detailed chemical kinetic model that includes subsets describing H_2/O_2, CO/CO_2, and NO_x chemistry; all presented within this paper. Each subset has been subjected to a critical review of available rate constant data, supplemented with rate constants determined from ab initio CBS-QB3 calculations. The work has lead to proposals of new, or updated, rate constants for a number of import reactions, e.g. $OH+HO_2 \rightleftharpoons H_2O+O_2$, $CO+OH \rightleftharpoons [HOCO] \rightleftharpoons CO_2+H$, $HOCO+OH \rightleftharpoons CO+H_2O_2$, $NO_2−H_2 \rightleftharpoons HNO_2+H$, $NO_2+HO_2 \rightleftharpoons HONO/HNO_2+O_2$, and $HNO_2(+M) \rightleftharpoons HONO$. Further validation of the model performance has been obtained through comparisons with flow reactor experiments from the literature on the chemical systems H_2/O_2, $H_2/O_2/NO_2$, and $CO/H_2O/O_2$ at 780–1100 K and 1–10 bar. Moreover, introduction of the reaction $CO+H_2O_2 \rightarrow HOCO+OH$ into the model yields an improved prediction, but no final resolution, to the recently debated syngas ignition delay problem compared to previous kinetic models.

BIBLIOGRAPHY

1. Mueller, M. A.; Yetter, R. A.; Dryer, F. L. Int J Chem Kinet 1999, 31, 113–125.
2. Mueller, M. A.; Yetter, R. A.; Dryer, F. L. Int J Chem Kinet 1999, 31, 705–724.
3. Amano, T.; Dryer, F. L. Proc Combust Inst 1998, 27, 397–404.
4. Held, T. J.; Dryer, F. L. Int J Chem Kinet 1998, 30, 805–830.
5. Curran, H. J.; Fischer, S. L.; Dryer, F. L. Int J Chem Kinet 2000, 32, 741–759.
6. Dagaut, P.; Cathonnet, M.; Rouan, J. P.; Foulatier, R.; Quilgars, A.; Boettner, J. C.; Gaillard, F.; James, H. J Phys E: Sci Instrum 1986, 19, 207–209.
7. Dagaut, P.; Boettner, J. C.; Cathonnet, M. Proc Combust Inst 1996, 26, 627–632.
8. Dagaut, P.; Dayma, G. Int J Hydrogen Energy 2006, 31, 505–515.

9. Mittal, G.; Sung, C.-J. Combust Sci Technol, 2007, 179, 497–530.

10. Mittal, G.; Sung, C.-J.; Fairweather, M.; Tomlin, A. S.; Griffiths, J. F.; Hughes, K. J. Proc Combust Inst 2007, 31, 419–427.

11. Walton, S. M.; He, X.; Zigler, B. T.; Wooldridge, M. S. Proc Combust Inst 2007, 31, 3147–3154.

12. Donovan, M. T.; He, X.; Zigler, B. T.; Palmer, T. R.; Wooldridge, M. S.; Atreya, A. Combust Flame 2004, 137, 351–365.

13. He, X.; Donovan, M. T.; Zigler, B. T.; Palmer, T. R.; Walton, S. M.; Wooldridge, M. S.; Atreya, A. Combust Flame 2005, 142, 266–275.

14. He, X.; Zigler, B. T.; Walton, S. M.; Wooldridge, M. S.; Atreya, A. Combust Flame 2006, 145, 552–570.

15. Huang, J.; Hill, P. G.; Bushe, W. K.; Munshi, S. R. Combust Flame 2004, 136, 25–42.

16. Huang, J.; Bushe, W. K.; Hill, P. G.; Munshi, S. R. Int J Chem Kinet 2006, 38, 221–233.

17. Tranter, R. S.; Raman, A.; Sivaramakrishnan, R.; Brezinsky, K. Int J Chem Kinet 2005, 37, 306–331.

18. Sivaramakrishnan, R.; Comandini, A.; Tranter, R. S.; Brezinsky, K.; Davis, S. G.; Wang, H. Proc Combust Inst 2007, 31, 429–437.

19. Petersen, E. L.; Davidson, D. F.; Hanson, R. K. Combust Flame 1999, 117, 272–290.

20. Petersen, E. L.; Kalitan, D. M.; Simmons, S.; Bourque, G.; Curran, H. J.; Simmie, J. M. Proc Combust Inst 2007, 31, 447–454.

21. Petersen, E. L.; Kalitan, D. M.; Barrett, A. B.; Reehal, S. C.; Mertens, J. D.; Beerer, D. J.; Hack, R. L.; McDonell, V. G. Combust Flame 2007, 149, 244–247.

22. Rytz, D. W.; Baiker, A. Ind Eng Chem Res 1991, 30, 2287–2292.

23. Ozturk, S.; Onal, I.; Senkan, S. Ind Eng Chem Res 2000, 39, 250–258.

24. Montgomery, J. A., Jr., Frisch, M. J.; Ochterski, J. W.; Petersson, G. A. J Chem Phys 1999, 110, 2822–2827.

25. Peng, D.-Y.; Robinson, D. B. Ind Eng Chem Fund 1976, 15, 59–64.

26. Elliott, J. R., Jr.; Lira, C. T. Introductory Chemical Engineering Thermodynamics; Prentice-Hall: Upper Saddle River, NJ, 1998.

27. Levenspiel, O. Chemical Reaction Engineering, 2nd ed.; Wiley: New York, 1972.

28. Levenspiel, O. The Chemical Reactor Omnibook; OSU Book Stores, Inc.: Corvallis, OR, 1993.

29. Taylor, G. Proc R Soc London, Ser A 1953, 219, 186–203.

30. Aris, R. Proc R Soc London, Ser A 1956, 235, 67–77.

31. Burcat, A.; Ruscic, B. Report TAE960, Technion Israel Institute of Technology, September 16, 2005.

32. Ruscic, B.; Pinzon, R. E.; Morton, M. L.; von Laszevski, G.; Bittner, S. J.; Nijsure, S. G.; Amin, K. A.; Minkoff, M.; Wagner, A. F. J Phys Chem A 2004, 108, 9979–9997.

33. Ruscic, B.; Pinzon, R. E.; Morton, M. L.; Srinivasan, N. K.; Su, M.-C.; Sutherland, J. W.; Michael, J. V. J Phys Chem A 2006, 110, 6592–6601.

34. Fabian, W. M. F.; Janoschek, R. J Mol Struct THEOCHEM 2005, 713, 227–234.

35. O'Conaire, M.; Curran, H. J.; Simmie, J. M.; Pitz, W. J.; Westbrook, C. K. Int J Chem Kinet 2004, 36, 603–622.

36. Li, J.; Zhao, Z.; Kazakov, A.; Dryer, F. L. Int J Chem Kinet 2004, 36, 566–575.

37. Hessler, J. P. J Phys Chem A 1998, 102, 4517–4526.

38. Hwang, S. M.; Ryu, S.-O.; De Witt, K. J.; Rabinowitz, M. J. Chem Phys Lett 2005, 408, 107–111.

39. Cobos, C. J.; Hippler, H.; Troe, J. J Phys Chem 1985, 89, 342–349.

40. Michael, J. V.; Su, M.-C.; Sutherland, J. W.; Carroll, J. J.; Wagner, A. F. J Phys Chem A 2002, 106, 5297–5313.

41. Baulch, D. L.; Bowman, C. T.; Cobos, C. J.; Cox, R. A.; Just, T.; Kerr, J. A.; Pilling, M. J.; Stocker, D.; Troe, J.; Tsang, W.; Walker, R. W.; Warnatz, J. J Phys Chem Ref Data 2005, 34, 757–1397.

42. Michael, J. V. Prog Energy Combust Sci 1992, 18, 327–347.

43. Srinivasan, N. K.; Michael, J. V. Int J Chem Kinet 2006, 38, 211–219.

44. Lifshitz, A.; Michael, J. V. Proc Combust Inst 1990, 23, 59–67.

45. Sutherland, J. W.; Patterson, P. M.; Klemm, R. B. Proc Combust Inst 1990, 23, 51–57.

46. Tsang, W.; Hampson, R. J Phys Chem Ref Data 1986, 15, 1087–1279.

47. Sridharan, U. C.; Qiu, L. X.; Kaufman, F. J Phys Chem 1982, 86, 4589–4574.

48. Keyser, L. F. J Phys Chem 1986, 90, 2994–3003.

49. Baldwin, R. R.; Fuller, M. E.; Hillman, J. S.; Jackson, D.; Walker, R. W. J Chem Soc, Faraday Trans 1 1974, 70, 635–641.

50. Michael, J. V.; Sutherland, J. W.; Harding, L. B.; Wagner, A. F. Proc Combust Inst 2000, 28, 1471–1478.

51. Keyser, L. F. J Phys Chem 1982, 86, 3439–3446.

52. Nicovich, J. M.; Wine, P. H. J Phys Chem 1987, 91, 5118–5123.

53. Friswell, N. J.; Sutton, M. M. Chem Phys Lett 1972, 15, 108–112.

54. Peeters, J.; Mahnen, G. Proc Combust Inst 1973, 14, 133–146.

55. DeMore, W. B. J Phys Chem 1979, 83, 1113–1118.

56. Burrows, J. P.; Cox, R. A.; Derwent, R. G. J Photochem 1981, 16, 147–168.

57. Cox, R. A.; Burrows, J. P.; Wallington, T. J Chem Phys Lett 1981, 84, 217–221.

58. Kurylo, M. J.; Klais, O.; Laufer, A. H. J Phys Chem 1981, 85, 3674–3678.

59. DeMore, W. B. J Phys Chem 1982, 86, 121–126.

60. Sridharan, U. C.; Qiu, L. X.; Kaufman, F. J Chem Phys 1984, 88, 1281–1282.

61. Keyser, L. F. J Phys Chem 1988, 92, 1193–1200.

62. Goodings, J. M.; Hayhurst, A. N. J Chem Soc, Faraday Trans 2 1988, 84, 745–762.

63. Hippler, H.; Troe, J.; Willner, J. J Chem Phys 1990, 93, 1755–1760.

64. Hippler, H.; Neunaber, H.; Troe, J. J Chem Phys 1995, 103, 3510–3516.

65. Kappel, C.; Luther, K.; Troe, J. Phys Chem Chem Phys 2002, 4, 4392–4398.

66. Srinivasan, N. K.; Su, M.-C.; Sutherland, J. W.; Michael, J. V.; Ruscic, B. J Phys Chem A 2006, 110, 6602–6607.

67. Baulch, D. L.; Cobos, C. J.; Cox, R. A.; Esser, C.; Frank, P.; Just, T.; Kerr, J. A.; Pilling, M. J.; Troe, J.; Walker, R. W.; Warnatz, J. J Phys Chem Ref Data 1992, 21, 411–734.

68. Atkinson, R.; Baulch, D. L.; Cox, R. A.; Hampson, R. F.; Kerr, J. A.; Troe, J. J Phys Chem Ref Data 1992, 21, 1125–1568.

69. Albers, E. A.; Hoyermann, K.; Wagner, H. G.; Wolfrum, J. Proc Combust Inst 1971, 13, 81–88.

70. Baldwin, R. R.; Brattan, D.; Tunnicliffe, B.; Walker, R. W.; Webster, S. J. Combust Flame 1970, 15, 133–142.

71. Klemm, R. B.; Payne, W. A.; Stief, L. J. Int J Chem Kinet 1975, 1, 61–72.

72. Wine, P. H.; Nicovich, J. M.; Thompson, R. J.; Ravishankara, A. R. J Phys Chem 1983, 87, 3948–3954.

73. Roscoe, J. M. Int J Chem Kinet 1982, 14, 471–478.

74. Hippler, H.; Troe, J. Chem Phys Lett 1992, 192, 333–337.

75. Sridharan, U. C.; Reimann, B.; Kaufman, F. J Chem Phys 1980, 73, 1286–1293.

76. Wine, P. H.; Semmes, D. H.; Ravishankara, A. R. J Chem Phys 1981, 75, 4390–4395.

77. Vaghjiani, G. L.; Ravishankara, A. R.; Cohen, N. J Phys Chem 1989, 93, 7833–7837.

78. Smith, I. W. M.; Zellner, R. J Chem Soc, Faraday Trans. 2 1973, 69, 1617–1627.

79. Smith, I. W. M. Chem Phys Lett 1977, 49, 112–115.

80. Ravishankara, A. R.; Thompson, R. L. Chem Phys Lett 1983, 99, 377–381.

81. Frost, M. J.; Sharkey, P.; Smith, I. W. M. J Phys Chem 1993, 97, 12254–12259.

82. Wooldridge, M. S.; Hanson, R. K.; Bowman, C. T. Proc Combust Inst 1994, 25, 741–748.

83. Fulle, D.; Hamann, H. F.; Hippler, H.; Troe, J. J Chem Phys 1996, 105, 983–1000.

84. Troe, J. Proc Combust Inst 1998, 27, 167–175.

85. Golden, D. M.; Smith, G. P.; McEwen, A. B.; Yu, C.-L.; Eiteneer, B.; Frenklach, M.; Vaghjiani, G. L.; Ravishankara, A. R.; Tully, F. P. J Phys Chem A 1998, 102, 8598–8606.

86. Ruscic, B.; Litorja, M. Chem Phys Lett 2000, 316, 45–50.

87. Duncan, T. V.; Miller, C. E. J Chem Phys 2000, 113, 5138–5140.

88. Yu, H. G.; Muckerman, J. T.; Sears, T. J Chem Phys Lett 2001, 349, 547–554.

89. Senosiain, J. P.; Musgrave, C. B.; Golden, D. M. Int J Chem Kinet 2003, 35, 464–474.

90. Senosiain, J. P.; Klippenstein, S. J.; Miller, J. A. Proc Combust Inst 2005, 30, 945–953.

91. Janoschek, R.; Rossi, M. J. Int J Chem Kinet 2004, 36, 661–686.

92. Bacskay, G. B.; Mackie, J. C. J Phys Chem A 2005, 109, 2019–2025.

93. Drummond, L. J. Aust J Chem 1968, 21, 2631.

94. Brabbs, T. A.; Belles, F. E.; Brokaw, R. S. Proc Combust Inst 1971, 13, 129.

95. Rawlins, W. T.; Gardiner, W. C., Jr.; J Phys Chem 1974, 78, 497–500.

96. Thielen, K.; Roth, P. Ber Bunsen-Ges Phys Chem 1983, 87, 920–925.

97. Clark, T. C.; Dean, A. M.; Kistiakowsky, G. B. J Chem Phys 1971, 54, 1726–1727.

98. Mittal, G.; Sung, C.-J.; Yetter, R. A. Int J Chem Kinet 2006, 38, 516–529.

99. Sun, H.; Yang, S. I.; Jomaas, G.; Law, C. K. Proc Combust Inst 2007, 31, 439–446.

100. You, X.; Wang, H.; Goos, E.; Sung, C.-J.; Klippenstein, S. J. J Phys Chem A 2007, 111, 4031–4042.

101. Yu, H. G.; Muckerman, J. T.; Francisco, J. S. J Phys Chem A 2005, 109, 5230–5236.

102. Nolte, J.; Grussdorf, J.; Temps, F.; Wagner, H. G. Z Naturforsch A: Phys Sci 1993, 48, 1234–1238.

103. Petty, J. T.; Harrison, J. A.; Moore, C. B. J Phys Chem 1993, 97, 11194–11198.

104. Miller, J. A.; Bowman, C. T. Prog Energy Combust Sci 1989, 15, 287–338.

105. Glarborg, P.; Dam-Johansen, K.; Miller, J. A. Int J Chem Kinet 1995, 27, 1207–1220.

106. Allen, M. T.; Yetter, R. A.; Dryer, F. L. Int J Chem Kinet 1995, 27, 883–909.

107. Allen, M. T.; Yetter, R. A.; Dryer, F. L. Combust Flame 1997, 109, 449–470.

108. Dean, A. M.; Bozzelli, J. W. In Combustion Chemistry of Nitrogen; Gardiner, W. C., Jr.; (Ed.); Springer-Verlag: New York, 2000; pp. 125–341.

109. Glarborg, P.; Alzueta, M. U.; Dam-Johansen, K.; Miller, J. A. Combust Flame 1998, 115, 1–27.

110. Glarborg, P.; Kristensen, P. G.; Dam-Johansen, K.; Alzueta, M. U.; Millera, A.; Bilbao, R. Energy Fuels 2000, 141, 828–838.

111. Skreiberg, Ø.; Kilpinen, P.; Glarborg, P. Combust Flame 2004, 136, 501–518.

112. Koch, T. G.; Sodeau, J. R. J Phys Chem 1995, 99, 10824–10829.

113. Nguyen, M. T.; Sumathi, R.; Sengupta, D.; Peeters, J. Chem Phys 1998, 230, 1–11.

114. Asatryan, R.; Bozzelli, J. W.; Simmie, J. M. Int J Chem Kinet 2007, 39, 378–398.

115. Chan, W.-T.; Heck, S. M.; Pritchard, H. O. Phys Chem Chem Phys 2001, 3, 56–62.

116. Eckart, C. Phys Rev 1930, 35, 1303–1309.

117. Endo, H.; Glänzer, K.; Troe, J. J Phys Chem 1979, 83, 2083–2090.

118. Yarwood, G.; Sutherland, J. W.; Wickramaaratchi, M. A.; Klemm, R. B. J Phys Chem 1991, 95, 8771–8775.

119. Röhrig, M.; Petersen, E. L.; Davidson, D. F.; Hanson, R. K. Int J Chem Kinet 1997, 29, 483–494.

120. Hippler, H.; Siefke, M.; Stark, H.; Troe, J. Phys Chem Chem Phys 1999, 1, 57–61.

121. Tsang, W.; Herron, J. J Phys Chem Ref Data 1991, 20, 609–663.

122. Ko, T.; Fontijn, A. J Phys Chem 1991, 95, 3984–3987.

123. Atkinson, R.; Baulch, D. L.; Cox, R. A.; Hampson, R. F.; Kerr, J. A.; Rossi, M. J.; Troe, J. J Phys Chem Ref Data 1997, 26, 1329–1499.

124. Bemand, P. P.; Clyne, M. A. A.; Watson, R. T. J Chem Soc Faraday Trans 2 1974, 70, 564–576.

125. Atkinson, R.; Baulch, D. L.; Cox, R. A.; Hampson, R. F.; Kerr, J. A.; Troe, J. J Phys Chem Ref Data 1989, 18, 881–1097.

126. Hahn, J.; Luther, K.; Troe, J Phys Chem Chem Phys 2000, 2, 5098–5104.

127. Forster, R.; Frost, M.; Fulle, D.; Hamann, H. F.; Hippler, H.; Schlepegrell, A.; Troe, J. J Chem Phys 1995, 103, 2949–2958.

128. Fulle, D.; Hamann, H. F.; Hippler, H.; Troe, J. J Chem Phys 1998, 108, 5391–5397.

129. Dransfield, T. J.; Perkins, K. K.; Donahue, N. M.; Anderson, J. G.; Sprengnether, M. M.; Demerjian, K. L. Geophys Res Lett 1999, 26, 687–690.

130. D'Ottone, L.; Campuzano-Jost, P.; Bauer, D.; Hynes, A. J. J Phys Chem A 2001, 105, 10538–10543.

131. Hippler, H.; Nasterlack, S.; Striebel, F. Phys Chem Chem Phys 2002, 4, 2959–2964.

132. Glänzer, K.; Troe, J. Ber Bunsen-Ges Phys Chem 1974, 78, 71–76.

133. Harrison, H.; Johnston, H. S.; Hardwick, E. R. J Am Chem Soc 1962, 84, 2478–2482.

134. Golden, D. M.; Smith, G. P. J Phys Chem A 2000, 104, 3991–3997.

135. Donahue, N. M.; Mohrschladt, R.; Dransfield, T. J.; Anderson, J. G.; Dubey, M. K. J Phys Chem A 2001, 105, 1515–1520.

136. Troe, J. Int J Chem Kinet 2001, 33, 878–889.

137. Glarborg, P.; Alzueta, M. U.; Kjaergaard, K.; Dam-Johansen, K. Combust Flame 2003, 115, 629–638.

138. Hori, M.; Matsunaga, N.; Marinov, N.; Pitz, W.; Westbrook, C. Proc Combust Inst 1998, 27, 389–396.

139. Tyndall, G. S.; Orlando, J. J.; Calvert, J. G. Environ Sci Technol 1995, 29, 202–206.

140. Glänzer, K.; Troe, J. Ber Bunsen-Ges Phys Chem 1975, 79, 465–469.

141. Chan, W.-T.; Pritchard, H. O. Phys Chem Chem Phys 2002, 4, 557–560.

142. Gierczak, T.; Jiménez, E.; Riffault, V.; Burkholder, J. B.; Ravishankara, A. R. J Phys Chem A 2005, 109, 586–596.

143. Slack, M. W.; Grillo, A. R. Combust Flame 1978, 31, 275–283.

144. Mueller, M. A.; Gatto, J. L.; Yetter, R. A.; Dryer, F. L. Combust Flame 2000, 120, 589–594.

145. Park, J.; Giles, N. D.; Moore, J.; Lin, M. C. J Phys Chem A 1998, 102, 10099–10105.

146. Hsu, C.-C.; Lin, M. C.; Mebel, A. M.; Melius, C. F. J Phys Chem A 1997, 101, 60–66.

147. Olbregts, J. Int J Chem Kinet 1985, 17, 835–848.

148. Milks, D.; Adams, T. N.; Matula, R. A. Combust Sci Technol 1979, 19, 151–159.

149. Freund, H.; Palmer, H. B. Int J Chem Kinet 1977, 9, 887–905.

150. Palmer, H. B.; Freund, H. Combust Sci Technol 1980, 21, 179–180.

151. Brown, F. B.; Crist, R. H. J Chem Phys 1941, 9, 840–846.

152. Johnston, H. S.; Bonner, W. A.; Wilson, D. J. J Chem Phys 1957, 26, 1002–1006.

153. Thomas, J. H.; Woodman, G. R. Trans Faraday Soc 1967, 63, 2728–2736.

154. Burcat, A.; Lifshitz, A. J Phys Chem 1970, 74, 263–268.

155. Burkholder, J. B.; Mellouki, A.; Talukdar, R.; Ravishankara, A. R. Int J Chem Kinet 1992, 24, 711–725.

156. Mebel, A. M.; Lin, M. C.; Morokuma, K. Int J Chem Kinet 1998, 30, 729–736.

157. Inomata, S.; Washida, N. J Phys Chem A 1999, 103, 5023–5031.

158. Xu, Z. F.; Lin, M. C. Int J Chem Kinet 2004, 36, 205–215.

159. Lutz, A. E.; Kee, R. J.; Miller, J. A. Sandia Report SAND87–8248·UC–401, Sandia National Laboratories, Livermore, CA, 1990.

160. Kee, R. J.; Rupley, F. M.; Miller, J. A. Sandia Report SAND89–8009B·UC–706, Sandia National Laboratories, Livermore, CA, 1989.

161. Yetter, R. A.; Dryer, F. L.; Rabitz, H. Combust Sci Technol 1991, 79, 129–140.

162. Baulch, D. L.; Cobos, C. J.; Cox, R. A.; Frank, P.; Hayman, G.; Just, T.; Kerr, J. A.; Murrells, T.; Pilling, M. J.; Troe, J.; Walker, R. W.; Warnatz, J. J Phys Chem Ref Data 1994, 23, 847–1033.

163. Davis, S. G.; Joshi, A. V.; Wang, H.; Egolfopoulos, F. Proc Combust Inst 2005, 30, 1283–1292.

164. Li, J.; Zhao, Z.; Kazakov, A.; Chaos, M.; Dryer, F. L.; Scire, J. J., Jr.; Int J Chem Kinet 2007, 39, 109–136.

165. Saxena, P.; Williams, F. A. Combust Flame 2006, 145, 316–323.

166. Peschke, W. T.; Spadaccini, L. J. Technical Report EPRI AP-4291, Electric Power Research Institute, Palo Alto, CA, 1985.

167. Dryer, F. L.; Chaos, M. Combust Flame 2008, 152, 293–298.

168. Cohen, N.; Westberg, K. R. J Phys Chem Ref Data 1983, 12, 531–590.

169. Troe, J. Proc Combust Inst 1975, 15, 667–680.

170. Westmoreland, P. R.; Howard, J. B.; Longwell, J. P. AIChE J 1986, 32, 1971–1979.

171. Riley, P. S.; Cosic, B.; Fontijn, A. Int J Chem Kinet 2003, 35, 374–380.

172. Becker, E.; Rahman, M. M.; Schindler, R. N. Ber Bunsen-Ges Phys Chem 1992, 96, 776–783.

173. DeMore, W. B.; Sander, S. P.; Goldena, D. M.; Molina, M. J.; Hampson, R. F.; Kurylo, M. J.; Howard, C. J.; Ravishankara, A. R. Technical Report JPL–PUBL–90–1, National Aeronautics and Space Administration, Jet Propulsion Laboratory, Pasadena, CA, 1990.

174. Soto, M. R.; Page, M. J Chem Phys 1992, 97, 7287–7296.

175. Soto, M. R.; Page, M.; McKee, M. L. Chem Phys 1991, 153, 415–426.

176. Bryukov, M. G.; Kachanov, A. A.; Timonnen, R.; Seetula, J.; Vandoren, J.; Sarkisov, O. M. Chem Phys Lett 1993, 208, 392–398.

177. Mebel, A. M.; Lin, M. C.; Melius, C. F. J Phys Chem A 1998, 102, 1803–1807.

178. Boughton, J. W.; Kristyan, S.; Lin, M. C. Chem Phys 1997, 214, 219–227.

179. Lamb, J. J.; Mozurkewich, M.; Benson, S. W. J Phys Chem 1984, 88, 6441–6448.